

An Alternative Approach to Mapping Pigments in Paintings With Hyperspectral Reflectance Image Cubes Using Artificial Intelligence

Tania Kleynhans (✉ tkpci@rit.edu)

Rochester Institute of Technology <https://orcid.org/0000-0003-4691-5129>

Catherine M. Schmidt Patterson

Getty Conservation Institute

Kathryn A. Dooley

National Gallery of Art, Washington, DC

David W. Messinger

Rochester Institute of Technology

John K. Delaney

National Gallery of Art, Washington, DC

Research article

Keywords: Reflectance imaging spectroscopy, Hyperspectral imaging, Convolutional neural network, Pigment mapping, Illuminated manuscripts

Posted Date: July 7th, 2020

DOI: <https://doi.org/10.21203/rs.3.rs-40103/v1>

License:  This work is licensed under a Creative Commons Attribution 4.0 International License.

[Read Full License](#)

Version of Record: A version of this preprint was published on August 18th, 2020. See the published version at <https://doi.org/10.1186/s40494-020-00427-7>.

RESEARCH

An alternative approach to mapping pigments in paintings with hyperspectral reflectance image cubes using artificial intelligence

Tania Kleynhans^{1*}, Catherine M. Schmidt Patterson², Kathryn A. Dooley³, David W. Messinger¹ and John K. Delaney³

*Correspondence: tkpci@rit.edu, j-delaney@nga.gov

¹Chester F. Carlson Center for Imaging Science, Rochester Institute of Technology, Lomb Memorial Drive, 14623 Rochester, NY, USA

Full list of author information is available at the end of the article

Abstract

Spectral imaging modalities, including reflectance and X-ray fluorescence, play an important role in conservation science. In reflectance hyperspectral imaging, the data are classified into areas having similar spectra and turned into labeled pigment maps using spectral features and fusing with other information. Direct classification and labeling remain challenging because many paints are intimate pigment mixtures that require a non-linear unmixing model for a robust solution. Neural networks have been successful in modeling non-linear mixtures in remote sensing with large training datasets. For paintings, however, existing spectral databases are small and do not encompass the diversity encountered. Given that painting practices are relatively consistent within schools of artistic practices, we tested the suitability of using reflectance spectra from a subgroup of well-characterized paintings to build a large database to train a one-dimensional (spectral) convolutional neural network. The labeled pigment maps produced were found to be robust within similar styles of paintings.

Keywords: Reflectance imaging spectroscopy; Hyperspectral imaging; Convolutional neural network; Pigment mapping; Illuminated manuscripts

1 Introduction

2 The development of spectral macroscale mapping modalities has provided conser-
3 vators, scientists and art historians with the ability to examine the distribution
4 of pigments across works of art with unprecedented detail. This allows for a more
5 robust understanding of an artist's creative process, and helps answer certain art

6 historical research questions. Importantly, it also informs conservators and muse-
7 ums on how to better preserve these works based on their materiality, propensity
8 for degradation, or even by identifying degradation products of processes already
9 occurring. The availability of pigment maps for a work of art, where each class is
10 labeled as a specific pigment or pigment mixture, greatly enhances the ability for
11 conservators to analyze paintings.

12 Currently the most widely used macroscale imaging modalities for art examination
13 are imaging X-ray fluorescence (XRF) spectroscopy [1], and reflectance hyperspec-
14 tral imaging (typically 400 to \sim 1000 nanometer (nm) and sometimes out to 2500
15 nm) [2], otherwise known as reflectance imaging spectroscopy (RIS). These two
16 modalities provide complementary information that can be used to identify and
17 map many of the pigments over a painting's surface [3]. Both modalities consist of
18 numerous narrow spectral band images, thus creating a 3-D image cube, where the
19 first two dimensions are spatial, and the third dimension is spectral. This produces
20 a spectrum at each spatial pixel in the image cube. The processing of these data
21 cubes has focused on grouping spatial pixels having similar spectral information,
22 allowing visualization of locations on a painted surface that may share a chemical
23 makeup. While XRF data can be processed readily to make elemental maps [4], the
24 direct translation of these into labeled pigment maps is, in general, not possible, as
25 the same element can often be found in more than one pigment (though exceptions
26 occur, such as the element mercury which can usually be assigned to the pigment
27 vermilion in a painted object). Analysis of RIS data cubes of paintings is more chal-
28 lenging, and has typically utilized workflows and algorithms developed for remote
29 sensing of minerals and vegetation.

30 Generally in remote sensing, the exploitation of reflectance image cubes to make
31 classification and/or material maps has been an active area of research for decades,
32 utilizing both physics-based and data-driven algorithms [5, 6, 7]. Classification maps
33 help segment large reflectance image cubes into a discrete set of representative spec-
34 tra (known as endmembers or classes). A classification map groups related spectra
35 that comprise a given class, but does not identify the specific materials present. A
36 material map goes further and identifies the specific materials (e.g. minerals) that
37 make up each class.

38 A typical workflow in remote sensing for automatically labeling classes into mate-
39 rials requires a priori knowledge of the area imaged, specifically, sufficient knowledge
40 of what materials are to be expected must be known so that the appropriate spectral
41 library of pure materials can be selected. Then one of a variety of algorithms can
42 be used to find the best library spectral match to the spectral endmember for each
43 class. This approach requires libraries that consist of a handful of spectra for each
44 known pure material in the area imaged [8, 9, 10]. The success of this approach is
45 limited when there are variations in the reflectance spectra of a material – such as
46 those caused by variation in particle size – in the area imaged that are not present
47 in the spectral library [11].

48 If the spectra are linearly mixed, that is if the endmember spectrum is from a
49 pixel that covered a portion of area imaged consisting of more than one material
50 that are spatially separated, then the endmember spectrum can be fit by an area-
51 weighted linear combination of the pure materials as found in the library. If however
52 the materials are mixed intimately, resulting in light that does not simply reflect
53 off one material and into the hyperspectral camera but instead is reflected and/or
54 absorbed by the other adjacent materials (i.e. scattering) before entering the camera,
55 then the measured spectrum is not in general a weighted linear sum.

56 For intimate mixtures a non-linear unmixing model is required to correctly assign
57 the materials present in each class and thus make an accurate material map [12].
58 Two types of models have evolved over time. The first are the physics-based models
59 that require knowledge of physical and optical properties of the materials in the
60 mixture, as well as information about the pigment stratigraphy [13, 14]. Approx-
61 imations are often made in such models to reduce the amount of detailed information
62 required.

63 Alternative data-driven models have evolved in part as a solution to these chal-
64 lenges of intimate mixing. Because neural networks and deep learning models can
65 model non-linear functions, these models have recently been applied to the remote
66 sensing RIS classification challenge with growing success [15, 16]. However, to create
67 accurate material maps with convolutional neural networks (CNN), large labeled
68 reflectance databases (training datasets) are required. Spectral signature libraries of
69 pure materials typically do not contain sufficient sample diversity to create robust
70 material maps when a class is comprised of an intimate mixture. Currently only a

71 handful of open-source, labeled, remote sensing RIS datasets are available for devel-
72 oping classification models, and they are limited to one area imaged with less than 20
73 unique classes each (e.g Salinas, Indian Pines, Pavia datasets [17]). Several studies
74 have been performed which indicate that neural networks can outperform tradi-
75 tional un-mixing methods when applied to RIS remote sensing data [18, 19, 20, 21].

76 To date the majority of RIS data sets of paintings have been analyzed with linear
77 mixing algorithms in order to create classification maps. The most commonly used
78 workflow is the Spectral Hourglass Wizard (SHW) in the Environment for Visualiz-
79 ing Images (ENVI) software [22, 23, 24]. The application of this workflow has been
80 most successful when identification of the clusters which define potential classes
81 is done manually, by an experienced user, in a reduced dimensional space with a
82 subset of the spectra from the RIS data cube. Such processing, while successful, is
83 also time-consuming [25, 2]. Other automatic and more rapid algorithms to gen-
84 erate the class maps have shown promise but tend to only find about 70 to 80%
85 of the classes in real paintings [25]. All of these algorithms utilized in these work-
86 flows assume linear mixing and mixtures of pigments are treated as a single paint
87 (a relatively consistent mixture of colored pigments) and hence a unique material.
88 Labeling of the paint classes into their component pigments (i.e., labeled pigment
89 maps) is done either by identifying characteristic reflectance spectral features or
90 by spatially fusing the class maps with results from other analytical methods (e.g.,
91 XRF, extended-range reflectance (near-ultraviolet, near-infrared, and mid-infrared),
92 and Raman spectroscopies) which provide more detailed chemical information.

93 Other approaches that have been explored in the analysis of RIS image cubes from
94 paintings skip the classification step in order to directly assign the pigments present.
95 Among these is the Kubelka-Munk model which can predict the reflectance spectra
96 for intimate mixtures of pigments in optically thick paint layers from a weighted
97 sum of the ratios of the absorption ($K(\lambda)$) and scattering ($S(\lambda)$) coefficients of each
98 pigment. The pigments in the mixtures are thus determined by a least squares fitting
99 of the unknown reflectance spectra using a library of $K(\lambda)$ and $S(\lambda)$ coefficients for
100 the pigments expected to be present. These approaches have yielded good success
101 for paint-outs and model paintings prepared from the pigments in the reference
102 library, but have had limited success on real paintings [26, 27]. This is likely due
103 to a variety of factors including the fact that in the visible spectrum region more

104 than one mixture of pigments can provide a good fit. An interesting proposed work-
105 around to this problem is the use of a neural network to pre-select the pigments
106 for the least squares fitting of the K & S parameters from a library [14]. The
107 wide array of artists' methods for achieving a particular visual appearance (such as
108 using a lower paint layer to create specific optical effects), however, rely on the use
109 of a variety of materials and mixtures used, pigment particle sizes, and paint layer
110 thicknesses, which present a major difficulty with implementing the Kubelka-Munk
111 approach.

112 Analysis of paintings by conservators and conservation scientists over the years
113 has documented the diversity of paintings by individual artists and artistic schools
114 throughout history. There is a widespread use of pigment mixtures and layered
115 paint structures (stratigraphies) in paintings from the late medieval through to the
116 current time. Artists used materials from different sources and often combined pure
117 pigments to expand the range of colors, or hues, available to them. In any given
118 area of a painting, there may be anywhere from a single layer of paint to a highly
119 complex stratigraphy of a preparatory or ground layer (often chalk or gypsum),
120 one or more paint layer(s), colored transparent glazes, and varnish layers. In RIS
121 the paint stratigraphy cannot be ignored since deeper layers can become visible in
122 the deep red to near-infrared spectral region ($\lambda > 600$ nm) owing to the decreased
123 electronic absorption and light scattering of the pigment particles. Since the layered
124 structure of a painting and the pigments that comprise each layer are not known in
125 advance, a priori physics-based modeling is challenging for these complex datasets,
126 especially since a robust open source two-parameter (absorption and scattering)
127 spectral library of pigments is not available (although reflectance spectra of paints
128 made using historical recipes pigments containing a limited number of pigments
129 have been measured) [28].

130 To overcome the limitations of applying physics-based models for intimate mix-
131 tures found in paintings (lack of sufficient information on the optical properties of
132 the pigments likely present and their stratigraphy), in this study we have chosen to
133 explore a single-step data-driven solution to pigment labeling of reflectance spec-
134 tra from RIS data. However, like the data-driven solutions for non-linear mixing in
135 remote sensing, a large training dataset is needed to train the network models. Fur-
136 thermore, the spectral training database for a neural network model must include

137 the cases of intimate pigment mixtures, making these databases even larger than
138 those for physics-based models.

139 While fine art painting is a highly creative human endeavor, examination of real
140 objects suggests that artists did follow some patterns in working with materials to
141 achieve desired colors and visual effects. For example, the fast-drying paints used in
142 tempera painting (painting using a water-soluble paint binder such as egg yolk or
143 gum arabic) could not be blended and reworked in the way that the slower drying
144 oil paints offered. With the adoption of drying oils, the number of paint layers
145 increased from a few to tens of layers. Materials also changed, minerals, plants and
146 insects provided many pigments before chemical manufacture of pigments in the
147 18th century dramatically changed what was available and used by artists. Thus,
148 in general, the pigments and pigment mixtures, paint thicknesses, and the number
149 of layers encountered in a painting is expected to vary with the materials available
150 and artistic practice at any point in time, and in a somewhat predictable manner.

151 The adherence to a set of practices, and use of particular sets of artist materials,
152 often overlaps with defined artistic schools (defined historically or geographically).
153 This fact offers a possible solution to making a robust training library for a data-
154 driven model for directly labeling pigment maps from RIS data cubes of paintings.
155 In this paper we explore the suitability of building a training dataset from regions of
156 well-characterized paintings for an end-to-end supervised one-dimensional convolu-
157 tional neural network (1D-CNN). Spectra from paints containing single or multiple
158 pigments are collected for the training library to incorporate the inherent variability
159 in the data. This leverages the inference that for a collection of related paintings,
160 artists follow a similar, but not identical, working process. Such training sets can
161 therefore be expected to contain most of the diversity in hue and intensity required
162 for robust classification, which is not found in pigment libraries. When new RIS im-
163 age cubes are processed using the 1D-CNN model, they will be labeled as containing
164 particular pigments, creating a material map in a single step.

165 To test the pigment maps created by the 1D-CNN model, test cases based on paint-
166 ings in 14th century illuminated manuscripts were used. The resulting 1D-CNN was
167 assessed in two ways. First, the model's mean-per-class-accuracy was computed to
168 evaluate the performance of the model. Secondly, the model's results were compared
169 to those obtained via the more common, two-step approach (spectral classification

170 followed by labeling of pigments present based on additional information) to verify
171 the accuracy of the model. Paintings from two illuminated manuscripts were used
172 to test the robustness of the model.

173 **Results**

174 **Data and Experimental Setup**

175 The workflow to create a neural network with an appropriate training dataset and
176 to produce labeled pigment maps of paintings is outlined in Figure 1 and consists
177 of four steps: 1) collect a sufficiently large spectral training dataset in which the
178 pigments for each spectra are labeled; 2) create a neural network to predict pigments
179 present in the input RIS spectra; 3) validate the accuracy of the network (predictions
180 of pigments present) with a hold-out sample (10% of the training data); and 4) test
181 the network prediction of pigments present on two well-characterized paintings that
182 were not part of the training dataset.

183 In order to build a reasonable pigment labeled reflectance spectral training dataset
184 for a given artistic school, paintings from which training data are selected must meet
185 several constraints. They must be painted using a similar suite of materials, and
186 generally with similar painting methods with respect to ground application (or ab-
187 sence thereof), degree of layering, degree of pigment mixing, etc. as described above.
188 They need not, necessarily, be painted by the same artist, so long as these general
189 criteria are met. Having reflectance data from the work of several artists who paint
190 using similar methods may make the training data more robust. Manuscript illumi-
191 nations (the painted images found within early books) have been widely analyzed by
192 RIS [29, 30, 41] and provide an ideal test case for the approach used here. We have
193 therefore selected paintings from a single book likely executed by a small number of
194 artists, all with access to similar pigments, and following similar painting techniques
195 with respect to pigment mixtures and glazes (that is, operating in the same general
196 school of artistic practice).

197 Additionally, the set of pigments used in manuscript illumination is relatively
198 limited, and well-studied, making it possible to confidently identify examples of
199 the most commonly encountered pigments, pigment mixtures, and painting tech-
200 niques [31, 32, 33, 34, 35]. For example, purple pigments can be derived from natural
201 materials such as mollusks, lichens or dye plants, or by using mixtures of blue pig-

202 ments (e.g. azurite, ultramarine, indigo) with red lake pigments (such as carminic
203 acid or brazilwood) to create purple hues. Similarly, blue pigments were often mixed
204 with yellow pigments (lead tin yellow or yellow dyes precipitated onto substrates)
205 to expand the range of copper-based green materials available to an illuminator.
206 The possible combinations of materials could create variation even within a single
207 object in the painting. To model the three-dimensional form of a blue azurite robe,
208 for example, lead white could be mixed in larger amounts to achieve highlights on
209 the robe, or a transparent red lake could be layered on top of the blue to define
210 purplish shadows. Both mixing and layering can contribute to the non-linear mixing
211 effects evident in reflectance spectra from such areas.

212 The reflectance training dataset created for the 1D-CNN consisted of spectra
213 collected from four well-characterized paintings from an illuminated manuscript
214 containing many of these commonly encountered materials and mixtures. The
215 manuscript chosen for this work was the *Laudario of Sant'Agnese* (c. 1340), one
216 of only three surviving illuminated books of this type (a laudario is a collection of
217 hymns of praise), and which has individual illuminations (described as paintings
218 throughout this paper for clarity) by at least two artists, which are now dispersed
219 in several collections around the world [36, 37, 38]. The paintings used to build the
220 training set (Figure S1) include:

- 221 1 *The Martyrdom of Saint Lawrence*, Pacino di Bonaguida, about 1340, Tem-
222 pera and gold leaf on parchment. The J. Paul Getty Museum, Los Angeles,
223 Ms. 80b (2006.13), verso
- 224 2 *The Ascension of Christ*, Pacino di Bonaguida, about 1340, Tempera and
225 gold leaf on parchment. The J. Paul Getty Museum, Los Angeles, Ms. 80a
226 (2005.26), verso
- 227 3 *The Nativity with the Annunciation to the Shepherds*, Master of the Dominican
228 Effigies, c. 1340, miniature on vellum, National Gallery of Art, Washington,
229 D.C., Rosenwald Collection, 1949.5.87
- 230 4 *Christ and the Virgin Enthroned with Forty Saints*, Master of the Dominican
231 Effigies, c.1340, miniature on vellum, National Gallery of Art, Washington,
232 D.C., Rosenwald Collection, 1959.16.2

233 These paintings from the *Laudario* have been studied in great detail to determine
234 the pigments and paint mixtures used as well as the artists' working methods. The

235 illuminations in the collection of the J. Paul Getty Museum were extensively studied
236 for the 2012-2013 exhibition *Florence at the Dawn of the Renaissance: Painting and*
237 *Illumination 1300-1350* using point-based analysis techniques (XRF, Raman spec-
238 troscopy and microscopic examination), broadband infrared imaging (900-1700 nm)
239 and ultraviolet light induced visible fluorescence photography [41]. More recently
240 these folios have been re-examined by RIS, XRF imaging, as well as point-based
241 fiber optic reflectance spectroscopy (350-2500 nm) for this work. The point analysis
242 data was combined with the RIS data and XRF maps to define regions of the data
243 cubes where similar pigments are present. The results of all of these studies have
244 been summarized in the supplementary Table S2. The two works in the collection
245 of the National Gallery of Art have also been previously studied for the Colour
246 Manuscript in the Making conference (2016, University of Cambridge) and the RIS
247 image cubes have been classified and labeled with the pigments determined to be
248 present either from the RIS spectra and/or from the results of site-specific XRF
249 and fiber optic reflectance spectroscopy (350-2500 nm) [30, 25].

250 In constructing the training spectral dataset, regions in the RIS cubes having
251 the same spectral shape and known pigment composition were selected both within
252 a given painting as well as among all four paintings. The labels of the training
253 dataset represent the pigment(s) whose spectral signature(s) dominate(s) the spec-
254 tra (i.e., with the effects of the substrate and presence of ad-mixed white pigments
255 included). Thus, an area containing mostly azurite will be described as belonging
256 to the pigment category “azurite” (even if there is a small quantity of, for example,
257 a white, black, or other-colored pigment), while an area containing a fairly equal
258 mixture of azurite and lead white might be described as “azurite/white” when the
259 amount of white present begins to noticeably alter the spectrum. As a result, the
260 training dataset incorporates the effects of variations in paint layer thicknesses and
261 mixtures that incorporate white pigments (lead white, chalk, etc). The only paint
262 mixture excluded in the training dataset is that of the flesh. The omission of the
263 flesh tones was done purposely as they represent a small area of the paintings and
264 their composition is known to differ among the artists who painted each painting
265 used for the training [41].

266 Figure 2 (a) displays a representative image indicating the locations from which
267 reflectance spectra were extracted from one of the paintings, *The Nativity with the*

268 *Annunciation to the Shepherds*. Selected areas were not averaged; each spectrum
269 was treated as an individual feature. In total, 25 classes (paints) were identified.
270 These classes consisted of both pure pigments (where “pure” is used to describe
271 paints where spectra are dominated by one pigment) or “mixed” pigments (where
272 there are two pigments contributing to the spectral signature). The mean spectra
273 of all classes can be seen in the Supplemental Material, Figure S2, and represent
274 the diversity of pigment and pigment mixtures observed in these paintings. A total
275 of more than 300,000 individual spectra were collected across all four paintings.

276 Since not all pigments or mixtures are as abundantly used as others, there were
277 several classes where a limited number of samples was collected (e.g. 40 green earth
278 vs. 61092 azurite samples per class). For the model to formulate general rules and
279 not over-train on the larger classes, the training data were reduced to 16,683 spec-
280 tra with the number of samples per class more evenly distributed. This was accom-
281 plished by iteratively removing similar spectra (based on Euclidean distance as a
282 measure of similarity) in order to conserve the variability in the training spectra.
283 Thus, for each class with more than 1000 spectra, a spectrum was selected at ran-
284 dom, and the 100 most similar spectra to the chosen spectrum were removed from
285 the class. This was repeated until each large class was reduced significantly. Class
286 sizes and labels can be seen in the supplemental Table S1. Figure 2 (b) displays
287 the reduced number of spectra of brown ochre; the dotted line shows the average
288 of all plotted spectra. The spectral variability within this pigment can clearly be
289 seen in the plot. The one distinct outlier visible, with higher reflectance from 400
290 to 550 nm, and was probably mis-labeled in the original collected training spectra.
291 Cases similar to this one, where one or more spectra in the training data may be
292 incorrectly identified as belonging to a given pigment category, is due to the method
293 used to extract spectra for the training data, wherein spectra from related areas
294 were defined with the same pigment category label. The mean spectrum of each
295 pigment category is plotted in supplemental Figure S2, and correspond well to the
296 expected reflectance curve of the pigment(s) named in the category label.

297 Performance Evaluation of the 1D-CNN Model

298 The degree of success of the 1D-CNN model was evaluated in two ways. The first
299 method was a quantitative model performance evaluation and examines the robust-

ness of the neural network itself. The second provided insight as to how well the 1D-CNN model produces accurate labeled pigment maps. This is done by comparing the resulting maps with those generated using the more traditional method (i.e classification of the same RIS cube using ENVI-SHW followed by labeling the classes in terms of pigments either from RIS spectral features or fusing the class maps with other data), described in this paper as truth maps.

Quantitative Model Performance Evaluation

The first method, to validate the performance of the neural network on the training set created using the four paintings, applied 10-fold cross-validation to estimate model performance, with results averaged. The k-fold cross-validation is a method used to evaluate machine learning models, where the training data is split into k groups. The 1D-CNN is then trained on k-1 groups and tested on the hold-out group. This is repeated for all k groups and the results averaged to produce a less biased estimate of the model's performance [39]. To calculate the results of each of the k models, mean-per-class-accuracy was used. This method, used when training data have unbalanced sets (classes with different amounts of training data), reports the average of the errors in each class, thus giving similar weight to each class and preventing larger classes from dominating results. Thus the mean per class accuracy for each of the 10 models created using cross-validation was averaged to calculate the final model performance.

The overall mean per-class accuracy (averaged across the 10-fold cross validation results) for the 1D-CNN was 98.7%. Results for each pigment or mixture class can be seen in the supplementary material Table S1. Model performance based on this metric shows very good results for all classes.

Comparison of 1D-CNN pigment labeled maps versus truth maps

After training, the 1D-CNN model was applied first to the *Pentecost*, Figure 3 (a), another painting from the Laudario of Sant'Agnese, the same illuminated book from which the paintings used to create the training dataset were obtained. The output of the 1D-CNN consists of 25 maps, one for each of the pigment classes in the training dataset. The intensity at each pixel in a given map is the probability of a match between the RIS spectra at that spatial pixel and the pigment class as determined by the 1D-CNN model. Each of the labeled pigment maps were thresholded to 0.99

332 or greater probability to construct the composite pigment labeled map in Figure 3
333 (d). This reduced the number of pigment-labeled classes from the possible 25 to
334 13. A high threshold of 0.99 was chosen to reduce the number of false-positive as-
335 signments. In the final composite pigment labeled map, the classes are color coded
336 and labels are given in Figure 3 (b). The black background represents spatial pixels
337 where none of the 25 labeled pigment classes had a probability at or above 0.99.
338 Inspection of the composite map and color image reveals not all of the pixels were
339 assigned to a pigment class. Decreasing the threshold from 0.99 to 0.85, as shown in
340 the supplementary material (Figure S3), did assign unclassified areas to the correct
341 pigments, but at the expense of increased false positive identifications (e.g. parch-
342 ment classified as lead tin yellow). As noted, the areas of flesh were not included
343 in the training datasets, thus no labels were assigned to the flesh. Nevertheless the
344 majority of the painted areas have been assigned to a labeled pigment class.

345 The composite color coded pigment labeled map of the *Pentecost* obtained using
346 the traditional methods, the truth map, is shown in Figure 3 (c) and labeled pig-
347 ments found in these classes is given in the 1st column in Figure 3 (b). A detailed
348 table summarizing the information used to identify the pigments in the spectral
349 classes found using the ENVI-SHW is given in the supplemental Table S2. The col-
350 ors of the labeled classes were chosen to roughly represent the color of the actual
351 paint. The 1D-CCN model's color composite map, displayed in Figure 3 (d), used
352 a color scheme where the same color is used as the truth map if pigments were
353 the same, which can also be seen in the second column of Figure 3 (b). Comparing
354 Figure 3 (c) and (d) (or the two columns of Figure 3 (b)) shows that the 1D-CNN
355 model correctly labeled the pigments in most of the paints. For example, the paints
356 dominated by a single pigment – azurite, lead tin yellow, gold, ochres, red lead,
357 vermilion, green earth and red lake – were all correctly labeled.

358 For mixed pigments the 1D-CNN model provided both correct and some incorrect
359 assignments. The 1D-CNN model correctly labeled pixels when the degree of satu-
360 ration of a color varied over a fairly large range, for example the high and medium
361 saturated blue robes. In both colors, the same primary pigment, azurite, was used
362 but mixed with varying amounts of lead white. For the two areas where ultramarine
363 and azurite were used together, the lighter portion of the dome directly above Mary
364 and the lighter blue robe of the apostle in the bottom right, the 1D-CNN model

365 only correctly labeled the lighter portion above Mary, but not the very pale (unsat-
366 urated) robe. Interestingly, the light blue robe of the apostle at the bottom right
367 of Figure 3 (d) identified a small feature represented by only a handful of spatial
368 pixels as part of the “Red lake” pigment category (shown in pink in Figure 3 (d))
369 , which at first glance, appears as though it might represent a miss-classification.
370 However, after further visual investigation, this allocation was confirmed: in the ar-
371 eas classified as “Red lake,” reflectance spectra do indeed indicate that an organic
372 red colorant may be present as a layer over the blue and lead white mixture to
373 render the shadow folds in the robe.

374 The green paints of the robes proved the most challenging for the 1D-CNN model.
375 The truth map as well as magnified examination of the painting shows a yellow
376 green-base layer onto which a deeper green paint was layered, which helps define
377 the three-dimensional shape of the green-robed figure at bottom center. The yellow-
378 green base paint was found to be a mixture of lead tin yellow (type II), ultramarine,
379 and likely a copper-containing green pigment (see supplemental Table S2) and the
380 deeper green as a mixture of lead tin yellow with an unknown copper green. Neither
381 of these mixtures is present in the training dataset, however visual inspection of the
382 mean spectra of the yellow-green paints in the dataset indicate the best spectral
383 match would be with lead tin yellow mixed with azurite, due to the weak reflectance
384 maximum at ~ 730 nm.

385 There are two other small details where the 1D-CNN provided pigment labels
386 which prompted further investigation. These are illustrated in Figure 4. The first
387 concerns the left vertical portion of the red border. The top, right, and bottom
388 part of the red outer border show a sharp inflection point at 564 nm, indicative
389 of red lead. The RIS spectrum of the left vertical border (as pointed out by the
390 green bifurcated arrow in Figure 4a) shows a sharp inflection at 558 nm consistent
391 with red lead, although blue shifted, but it also shows a weak reflectance peak at
392 approximately 740 nm and rising reflectance starting at 850 nm.

393 These results suggest the presence of a second pigment along the red outer border
394 although assignment by RIS alone is not possible. The 1D-CNN model recognized a
395 difference between the left edge and the other sides of the red outer border, although
396 it labels the left edge as ochre, rather than red lead, azurite. Inspection of the copper
397 (Cu) elemental distribution map obtained from XRF mapping shows that copper

398 is associated with the blue azurite inner border. On the border's left edge, copper
399 is present in a wider line than what is currently visible in the color image, and
400 indicates azurite is present below the left portion of the red outer border. Visual
401 inspection of the color image shows some blue paint is just visible at the top edge
402 of the border (green arrow) (Figure 4(b)). Thus, while not correctly assigning the
403 pigments (since this combination of red lead and azurite was not in the training
404 dataset), the 1D-CNN model did assign the most logical pigment based on the RIS
405 features, and correctly noted the distinction between this area and the remainder
406 of the red lead border.

407 The second detail of interest is the shadowed side of the white square spire (Fig-
408 ure 4 (d,e,f)) which appears as a light gray blue in the color image and was labeled
409 as "indigo" by the 1D-CNN model, shown in teal in detail in Figure 4 (d). This area
410 appears to actually contain a small amount of a copper-containing pigment (likely
411 azurite, since the area has a blue-gray cast), as suggested by the copper distribution
412 obtained from XRF imaging (in Figure 4 (f)). This shadowed area was missed in the
413 classification step for the truth model. Spectra from this area have an overall lower
414 reflectance (by a factor of 2) and weak absorption features that suggest a small
415 amount of earth pigment was additionally added to the white. Taken together, the
416 RIS and XRF data suggests that the area may actually be a complex mixture of
417 lead white, ochre, and trace amounts of azurite. This three-part mixture is not in
418 the training set, so although the shadowed side of the spire was incorrectly ascribed
419 to the indigo class, the 1D-CNN model distinguished a difference between this area
420 and the rest of the white spire.

421 To further test the robustness of the 1D-CNN model a second painting, which
422 comes from a Choir Book (Gradual) series painted by Lippo Vanni, *Saint Peter*
423 *Enthroned*, c. 1345/1350, was analyzed. Vanni, while from Sienna rather than Flo-
424 rence, is likely to have been familiar with the painting techniques and pigments used
425 by the Florentine artists who did the paintings for the *Laudario of Sant'Agnese*.

426 As in the case of the *Pentecost*, a pigment-labeled truth map was constructed
427 from first creating classification maps based on RIS spectra (400 to 950 nm) using
428 the ENVI-SHW algorithm and then by fusing results from point analysis methods
429 in order to turn the classification maps into labeled pigment maps (see supplement
430 Table S3 for details). The 1D-CNN model was applied to *Saint Peter Enthroned*

431 to determine the model’s generalizability to a painting not in the *Laudario*, but
432 which is expected to contain similar materials. The reference color image, truth
433 and 1D-CNN composite maps along with the color-coded pigment labels are given
434 in Figure 5. The data demonstrate that the paints dominated by a single pigment
435 were correctly identified even when lead white was present. Specifically the areas
436 containing azurite, lead white, vermilion, and red lake were all correctly labeled.
437 The areas of gold leaf, and the areas of exposed bole where the gold leaf is gone,
438 were also correctly identified as gold and ochre (the primary coloring material of
439 the clay bole underneath the gold), respectively. The 1D-CNN model incorrectly
440 labeled the yellow as lead tin yellow although the truth pigment map indicates
441 that a yellow lake is present, however yellow lakes are not present in the training
442 dataset. The truth map shows the dark modeling of the richly decorated red cloth
443 over St. Peter’s throne was painted with vermilion while the lighter parts were
444 painted with a mixture of vermilion and red lead. The 1D-CNN model correctly
445 labeled the vermilion. However, the mixture was labeled as only containing red lead
446 because these areas had sufficient red lead character to differentiate them from pure
447 vermilion, since the mixture was not in the training set.

448 There are three sets of mixed pigments in *Saint Peter Enthroned*, two greens and
449 an orange-red. As shown in the truth map, the green paints (Figure 5 (c)) are made
450 from a yellow lake with azurite denoted with a lighter green, and with a yellow lake,
451 azurite, and indigo for the cooler, darker green. The labeled pigments returned from
452 the 1D-CNN model (Figure 5 (d)) returned two greens composed of a yellow mixed
453 with a blue pigment and the model returned the correct blue pigment in both cases.
454 However, since no mixture of a yellow lake with these two blue pigments existed
455 in the training data, the model gave as the best match lead tin yellow mixed with
456 the specific blue pigment. This is not surprising as the spectral shape is dominated
457 by the blue pigment present. The labeled composite truth map shows that the
458 red border contains a mixture of red lead and vermilion, just like the lighter red
459 portion of the cloth over the throne. The 1D-CNN model correctly identified these
460 two pigments individually in the border, identifying primarily red lead on the right
461 side of the image, and vermilion on the far left. The model did not classify them as
462 a mixture since there was no mixed red lead and vermilion class in the model. This
463 result reinforces the notion that identification from the model can only be as exact

464 as the training data. As such, these results will always need to be presented with
465 some indication as to the limits of interpretability. However, as more paintings are
466 studied, the training set can be augmented to develop a more robust solution.

467 **Discussion**

468 The objective of this research was to determine if a data driven, rather than a
469 physics-based, solution to pigment labeling of reflectance spectra would be suffi-
470 cient. The motivation for testing this was not because physics-based solutions to
471 intimate mixing are not robust enough, but rather because obtaining the infor-
472 mation to implement the physics models are challenging due to the complexity of
473 paintings. Specifically, obtaining the optical properties of the pigments used, the
474 optical thickness of paint layers present and accounting for the possibility of glazes
475 over the paint layers pose difficulties. While destructive micro sampling can provide
476 such information, even well-studied paintings are sparsely sampled and no robust
477 non-invasive methods exist currently to obtain these parameters across the surface
478 of a painting. The data-driven solution explored here gets around this problem but
479 requires a large pigment labeled dataset, as all learning frameworks do.

480 The approach taken here is to constrain the size of the training dataset by de-
481 veloping them for specific artistic schools, which are often defined by a rough set
482 of pigments and subset of mixtures and more specific painting processes. That is,
483 only subsets of mixtures and layering are expected within these schools instead
484 of all possible combinations. Finally, rather than attempting to build a robust
485 training dataset by making contemporary paint-outs, the central idea is to utilize
486 well-characterized historic paintings to define a number of classes and encompass
487 the needed diversity, while simultaneously ensuring the use of historic pigments,
488 supports (such as parchment), and paintings grounds. This approach is inherently
489 attractive because it leverages the large amount of existing scientific data on par-
490 ticular paintings, suggesting that enough truth information is available to allow the
491 creation of appropriate training datasets for a number of artistic schools. Where
492 the predictions of labeled spectra break down using this approach, the dataset can
493 be refined, but the “failures” are likely new areas worthy of further study.

494 The limitations of this approach are twofold. First, it cannot be expected to work
495 well on all paintings, given that many exist at the boundaries between schools of

496 artistic practice. However, the understanding of a given artist or artistic school does
497 not require a rigorous understanding of each set of work in the school, but more often
498 the common elements between them and where they differ. The approach proposed
499 here, even with its limitations, is consistent with these goals. The second limitation
500 is that while a physics-based model can give concentrations of the pigments, the
501 data-driven approach to directly label pigments proposed here will not. Nor will the
502 proposed data-driven approach provide quantitative information about the mixtures
503 present nor find all the pigments present. Physics-based models are better suited
504 for these goals. However, in the conservation and art historical fields there has been
505 limited need for such detailed information, except for a small class of paintings where
506 the degradation over time has resulted in large imbalances in the color appearance
507 of specific pigments. In these cases, the focus is typically on getting quantitative
508 information for one or two specific pigments based on highly detailed studies, not of
509 the whole painting. For the vast majority of studies, then, the lack of quantitative
510 data is unlikely to be a hindrance to uptake of the method.

511 In this paper the proposed data-driven approach for the analysis of RIS image
512 cubes was applied to four well studied paintings from the same book, which could
513 be well-described by 25 pigment labeled classes, were sufficient to build the training
514 dataset for 14th century paintings found in illuminated books from the early Italian
515 Renaissance by artists in or near Florence. The trained 1D-CNN model was then
516 applied to a painting from the same book that contained the four paintings used for
517 training, as well as a painting from a different book and artist who worked outside of
518 Florence in Siena. Results were encouraging when compared with truth which was
519 obtained by labor intensive analysis by expert users. This makes it likely to become
520 a valuable addition to the workflow of museum-based scientists and conservators.

521 For both of the tested paintings, the 1D-CNN model correctly labeled all but one
522 of the classes in which a single pigment dominated the reflectance spectra. Of the 28
523 truth pigment allocations across both paintings (17 in the *Pentecost* and 11 in the
524 *Saint Peter Enthroned*), the 1D-CNN model correctly identified 19. However, of the
525 9 incorrectly classified pigments/mixtures, 7 were not part of the training dataset.
526 When these incorrect (but not surprising) classifications are discounted, the model
527 misclassified only 2 classes. These results point to a limitation of the 1D-CNN model,
528 as with most artificial intelligence models, that when a pigment is encountered for

529 which the model was not trained on, for example the yellow lake that was labeled as
530 lead tin yellow, the model fails. The model handles well cases where pure pigments
531 were mixed with varying amounts of lead white, and thus appears to be robust in
532 situations when the saturation is varied, so long as these cases are in the training
533 data. The model also handles the combination of ultramarine and azurite except for
534 the case when the pigment concentration was low and the color very light. Between
535 the two paintings there were four green paints made from mixtures. In each case,
536 the 1D-CNN model labeled the greens partially correctly, owing to not having the
537 right mixtures in the training data. Overall, the 1D-CNN model handled mixtures it
538 was trained for well, and found matches that were spectrally reasonable for those it
539 was not trained for. This illustrates both a benefit and risk. While the risk is clear
540 (like all data-driven models, there is chance for model predictions to be wrong),
541 the benefit is less obvious, but is particularly valuable in the field of art analysis.
542 Fundamentally, incorrect assignments provide a place to start from to improve the
543 training data. But it also provides an incentive for further research. In this work,
544 the case where the model was wrong, such as assigning an ochre where red lead
545 was expected in the red outer border, caused us to look more closely at this area,
546 making close comparisons to other data and reexamining the painting itself, to find
547 that the left edge of the border was painted over what was an “error” made by
548 the artist while painting the inner azurite blue border. Hence such errors can be
549 informative, particularly in cases where the examination of an object with RIS is
550 the first step of several analysis methods. This is, indeed, the case in many cultural
551 heritage studies.

552 Improving the training dataset is an iterative process and one that would improve
553 the performance here. The challenge is to look at more complex mixtures and layers
554 that arises from inherent variability of artists’ technique – including idiosyncratic
555 mixtures and/or layering methods that one artist may apply – which may exclude
556 the possibility of ever having a training set that can encompass all possible pigment
557 mixtures. For example, the artists considered in this work employ different pigments
558 and/or subtly different methods of painting flesh tones, depending on medium (e.g.
559 painting on parchment vs. panel paintings), size, and/or moment in their artistic
560 development; the extent to which this technique varies object-to-object and artist-
561 to-artist continues to be a subject of study [40, 41]. The expected variation of flesh

562 tone painting techniques suggests that, even within a single artistic tradition, some
563 natural variability may make some paint compositions more difficult to identify
564 than others, directly linked to whether an example is present in the training data.
565 As noted in the results section, three-component mixtures similarly find use, and
566 the lack of them in the training data provided one limit to the overall accuracy of
567 the 1D-CNN predictions. Therefore, adding more unique mixtures will undoubtedly
568 improve the results of the model. For example adding examples of the fleshtones
569 represented in the manuscripts studied here.

570 To extend the model beyond this artistic tradition, of course, will require addi-
571 tional extensions: for example, a similar model could reasonably be built to examine
572 19th or 20th century oil paintings, but would necessarily require a different train-
573 ing dataset, and be subject to the same challenges as demonstrated here for 14th
574 century illuminated manuscript paintings.

575 Even without these extensions, however, the potential to rapidly classify pigments
576 in a collection of works of art from the same painter (or painters from the same gen-
577 eral era and style), based on a model trained on a few well characterized paintings,
578 creates the opportunity for classification and analysis of an entire collection within
579 a short period of time and with less need for a trained expert user to supervise
580 the initial labeling process of an unknown painting. As such, the 1D-CNN model
581 provides an excellent first-pass analysis to help guide the researcher, and/or identify
582 areas deserving of more focused study by an expert user or which will require addi-
583 tional detailed analysis by other analytical techniques. An example of this kind of
584 highlighting of areas of interest include the initially painted portion of the border,
585 and the shading of the spires in the *Pentecost* from the *Laudario*. This application
586 of a 1D-CNN model, therefore, is expected to help conservators and conservation
587 scientists more rapidly evaluate the materialty of objects under their care, allowing
588 more rapid decision-making with respect to treatment and preservation options, as
589 well as identifying areas of ongoing interest or concern.

590 **Materials and Methods**

591 Reflectance Imaging Spectroscopy Data Collection

592 The RIS data used for creating the training dataset consisted of 209 spectral bands
593 that ranged from the visible to near infrared (400 to 950 nm). The resulting image

594 cube (2 spatial and 1 spectral dimension) were calibrated to apparent reflectance by
595 subtracting a dark image from the collected reflectance data in digital counts, and
596 dividing it by the illumination irradiance. The spectral component of the reflectance
597 spectrum at each pixel was used as input features (model input data) to the 1D-
598 CNN model.

599 Network Architecture

600 The 1D-CNN consists of 4 hidden layers. The architecture is displayed in Figure 6.
601 The input layer receives the initial data, which is the individual (labeled) spec-
602 tra collected from the studied paintings. The first two hidden layers have two 1D
603 convolutional layers with respectively 64 and 32 filters and kernel sizes of 5x5 and
604 3x3. This is followed by max pooling, where the hidden layers are down-sampled to
605 reduce their dimensionality, keeping the maximum output of each second feature.
606 Two fully connected (dense) layers of sizes 100 and 25 form the last two hidden
607 layers. Each hidden layer uses the rectified linear unit (ReLU) activation function
608 $f(x) = \max(0, x)$, thus retaining only the positive part of its input. The final output
609 activation function, Softmax, takes the output values and changes them to prob-
610 abilities between 0 and 1 with $f(s)_i = \frac{e^{s_i}}{\sum_j e_j^s}$ where s_i is the score inferred by the
611 neural net for each class in C . For this study, $C = 25$.

612 The performance of the model was measured with categorical cross-entropy loss
613 (log loss) function defined as $CE = -\sum_i^C t_i \log(s_i)$, where t_i is the ground truth
614 (label), and s_i the scores of the model for each class. For the categorical cross-
615 entropy loss calculation (compared to binary cross-entropy), each label was coded
616 as a one-hot vector since the neural network requires the label to be numeric. A
617 one-hot vector is a zero vector the length of the number of classes, with the class
618 represented as a 1 at the specific label number.

619 The model was trained with batch sizes of 50, and evaluated on a validation
620 set of 10% of the training data. The training started with a learning rate of 0.01,
621 which was decreased if after 4 epochs (cycle through full training dataset) the
622 validation loss did not decrease. The model used the stochastic gradient descent
623 optimizer to minimize the loss function. The neural network was coded in Python
624 using TensorFlow's Keras library [42].

625 Performance Evaluation Calculation

626 The 1D-CNN model accuracy was measured using the individual per-class results
627 from 10-fold cross validation. Thus the overall accuracy of the model was calcu-
628 lated by averaging the mean-per-class results for each of the 10 cross-validation
629 results. The mean-per-class accuracy measure is used when there are unbalanced
630 sets (classes with different volumes of data).

631 Three additional classification methods were tested to compare the 1D-CNN
632 model with alternative models commonly used for such datasets, namely 1) a Mul-
633 tilayer Perceptron (MLP) [43], 2) Support Vector Machine with radial basis kernel
634 (SVM) [44], and 3) Spectral Angle Mapper (SAM) to assign the class with the
635 smallest angle between the spectral library and each spectrum in the image. The
636 1D-CNN outperformed the others by 1.3% (MLP), 2.1% (SAM), and 6.4% (SVM)
637 mean per-class accuracy respectively.

638 Point-based Fiber Optic Reflectance Spectroscopy

639 FORS spectra were collected in a non-contact configuration using an ASD Field
640 Spec3 (Malvern Panalytical) which is sensitive from 350–2500 nm. The collection
641 fiber is oriented at approximately 90 degrees to the painting surface, resulting in a
642 collection spot size approximately 3 mm in diameter, and the illumination source is
643 held approximately 10 cm from the surface at a 45 degree angle. The total acquisi-
644 tion time was less than 6 seconds per spot. The light level was approximately 5000
645 lux.

646 Scanning XRF spectroscopy

647 Scanning MA-XRF spectroscopy is a non-contact chemical imaging technique which
648 captures information about the elemental composition of a two-dimensional area.
649 In many cases, the pigments, metals, and other materials present in a work of art
650 can be inferred from the elemental composition. Since the technique is X-ray-based,
651 the elemental distributions often captures both surface and sub-surface information
652 simultaneously. In MA-XRF-derived element distribution maps, brighter areas rep-
653 resent higher signal from an element. In this study, scanning XRF spectroscopy was
654 done at the Getty Conservation Institute (GCI) using a Bruker M6 Jetstream (Rh
655 tube, operated at 50 kV/400 μ A, 450 μ m spot size, 440 μ m sampling and a dwell
656 time of 18 ms/pixel). A corrected excitation spectrum of the instrument was mea-

657 sured by Timo Wolff and data processing utilized the PyMCA and DataMuncher
658 software suites.[45, 4, 46] The total area scanned on the *Pentecost* (not shown) was
659 316×404 mm; details shown in Figure 4 show spatial subsets of this scan, with
660 histograms stretched to emphasize weak features.

661 **Abbreviations**

662 **nm:** Nanometer

663 **XRF:** X-ray fluorescence

664 **RIS:** Reflectance imaging spectroscopy

665 **CNN:** Convolutional neural network

666 **SHW:** Spectral Hourglass Wizard

667 **ENVI:** Environment for Visualizing Images

668 **1D-CNN:** One-dimensional convolutional neural network

669 **Cu:** Copper

670 **ReLU:** Rectified linear unit

671 **MLP:** Multilayer perceptron

672 **SVM:** Support vector machine

673 **SAM:** Spectral angle mapper

674 **Availability of data and materials**

675 The datasets used and/or analyzed during the current study may be made available from the authors on reasonable
676 request.

677 **Competing interests**

678 The authors declare that they have no competing interests.

679 **Author's contributions**

680 TK and JKD conceived the research. TK developed, programmed, trained, and tested the neural network and
681 automatic spectral angle mapping algorithms. JKD, CMSP and KAD collected the RIS, XRF data sets and did the
682 analyses needed for the verification “truth data” sets. DWM oversaw all of the analysis methods. All authors wrote
683 the manuscript.

684 **Funding**

685 This work was supported in part by the Rochester Institute of Technology, College of Science, Dean's Research
686 Initiation Grant (TK), the National Gallery of Art (JKD, KAD), and the Getty Conservation Institute (CMSP).

687 **Acknowledgements**

688 We thank Paola Ricciardi, Lisha Glinsman, Kathryn Morales, and Michelle Facini for XRF data collection and
689 analysis of the NGA paintings. We would also like to thank Nancy Turner and Bryan Keene (J. Paul Getty Museum)
690 for helpful discussion.

691 **Author details**

692 ¹Chester F. Carlson Center for Imaging Science, Rochester Institute of Technology, Lomb Memorial Drive, 14623
693 Rochester, NY, USA. ²Getty Conservation Institute, Getty Center Dr, 90049 Los Angeles, CA, USA. ³National
694 Gallery of Art, 6th and Constitution Avenue NW, 20565 Washington, DC, USA.

695 **References**

- 696 1. M. Alfeld, K. Janssens, J. Dik, W. de Nolf, G. van der Snickt, Optimization of mobile scanning macro-xrf
697 systems for the in situ investigation of historical paintings. *Journal of Analytical Atomic Spectrometry*
698 **26**, 899-909 (2011).
- 699 2. J. K. Delaney, J. G. Zeibel, M. Thoury, R. Littleton, M. Palmer, K. M. Morales, E. R. de la Rie,
700 A. Hoenigswald, Visible and infrared imaging spectroscopy of Picasso's Harlequin Musician: Mapping and
701 identification of artist materials in situ. *Applied Spectroscopy* **64**, 584 – 594 (2010).

- 702 3. K. Dooley, D. Conover, L. Glinsman, J. Delaney, Complementary standoff chemical imaging to map and
703 identify artist materials in an early Italian Renaissance panel painting. *Angewandte Chemie International*
704 *Edition* **126** (2014).
- 705 4. M. Alfeld, K. Janssens, Strategies for processing mega-pixel X-ray fluorescence hyperspectral data: a case study
706 on a version of Caravaggio's painting Supper at Emmaus. *J. Anal. At. Spectrom.* **30**, 777-789 (2015).
- 707 5. J.-B. Feret, C. François, G. P. Asner, A. A. Gitelson, R. E. Martin, L. P. Bidet, S. L. Ustin, G. le Maire,
708 S. Jacquemoud, PROSPECT-4 and 5: Advances in the leaf optical properties model separating photosynthetic
709 pigments. *Remote Sensing of Environment* **112**, 3030 - 3043 (2008).
- 710 6. S. Schneider, A. Melkumyan, R. J. Murphy, E. Nettleton, Gaussian Processes with OAD covariance function for
711 hyperspectral data classification. *22nd IEEE International Conference on Tools with Artificial*
712 *Intelligence* (2010), vol. 1, pp. 393-400.
- 713 7. J. Verrelst, L. Alonso, G. Camps-Valls, J. Delegido, J. Moreno, Retrieval of vegetation biophysical parameters
714 Using Gaussian process techniques. *IEEE Transactions on Geoscience and Remote Sensing* **50**,
715 1832-1843 (2012).
- 716 8. A. Mende, U. Heiden, M. Bachmann, D. Hoja, M. Buchroithner, Development of a new spectral library
717 classifier for airborne hyperspectral images on heterogeneous environments. *Proceedings of the EARSeL*
718 *7th SIG-Imaging Spectroscopy Workshop* (2011).
- 719 9. N. R. Rao, P. K. Garg, S. K. Ghosh, Development of an agricultural crops spectral library and classification of
720 crops at cultivar level using hyperspectral data. *Precision Agriculture* **8**, 173-185 (2007).
- 721 10. S. Vishnu, R. R. Nidamanuri, R. Bremananth, Spectral material mapping using hyperspectral imagery: a review
722 of spectral matching and library search methods. *Geocarto International* **28**, 171-190 (2013).
- 723 11. R. N. Clark, Spectroscopy of Rocks and Minerals, and Principles of Spectroscopy, *The Oxford Handbook of*
724 *Innovation*, R. A. R. Andrew N. Rencz, ed. (John Wiley and Sons, New York), chap. 1, 3-58 (1999).
- 725 12. R. Heylen, M. Parente, P. D. Gader, A Review of Nonlinear Hyperspectral Unmixing Methods. *IEEE Journal*
726 *of Selected Topics in Applied Earth Observations and Remote Sensing* **7**, 1844-1868 (2014).
- 727 13. Abu Md Niamul Taufique, D. W. Messinger, *Algorithms, technologies, and applications for*
728 *multispectral and hyperspectral imagery XXV*, M. Velez-Reyes, D. W. Messinger, eds., International
729 Society for Optics and Photonics (SPIE), **10986**, 297-307 (2019).
- 730 14. N. Rohani, E. Pouyet, M. Walton, O. Cossairt, A. K. Katsaggelos, Nonlinear unmixing of hyperspectral
731 datasets for the study of painted works of art. *Angewandte Chemie* **130**, 11076-11080 (2018).
- 732 15. Y. Han, Y. Gao, Y. Zhang, J. Wang, S. Yang, Hyperspectral sea ice image classification based on the
733 spectral-spatial-joint feature with deep learning. *Remote Sensing* **11**, 2170 (2019).
- 734 16. L. Ma, Y. Liu, X. Zhang, Y. Ye, G. Yin, B. Johnson, Deep learning in remote sensing applications: A
735 meta-analysis and review. *ISPRS Journal of Photogrammetry and Remote Sensing* **152**, 166-177
736 (2019).
- 737 17. Datasets for Classification. <http://lesun.weebly.com/hyperspectral-data-set.html>, Accessed: 20 June
738 2020.
- 739 18. G. A. Licciardi, F. Del Frate, Pixel unmixing in hyperspectral data by means of neural networks. *IEEE*
740 *Transactions on Geoscience and Remote Sensing* **49**, 4163-4172 (2011).
- 741 19. X. Zhang, Y. Sun, J. Zhang, P. Wu, L. Jiao, Hyperspectral unmixing via deep convolutional neural networks.
742 *IEEE Geoscience and Remote Sensing Letters* **15**, 1755-1759 (2018).
- 743 20. M. Wang, M. Zhao, J. Chen, S. Rahardja, Nonlinear unmixing of hyperspectral data via deep autoencoder
744 networks. *IEEE Geoscience and Remote Sensing Letters* **16**, 1467-1471 (2019).
- 745 21. L. Qi, J. Li, Y. Wang, M. Lei, X. Gao, Deep spectral convolution network for hyperspectral image unmixing
746 with spectral library. *Signal Processing* p. 107672 (2020).
- 747 22. L3 Harris Geospatial Solutions, Spectral Hourglass Wizard.
748 <https://www.harrisgeospatial.com/docs/SpectralHourglassWizard.html>, Accessed: 6 June 2020.
- 749 23. Y. Arvelyna, M. Shuichi, M. Atsushi, A. Nguno, K. Mhopjeni, A. Muyongo, M. Sibeso, E. Muvangua, *IEEE*
750 *International Geoscience and Remote Sensing Symposium* , 1752-1754 (2011).
- 751 24. K. D. Singh, Automated spectral mapping and subpixel classification in the part of Thar Desert using EO-1
752 satellite Hyperion data. *IEEE Geoscience and Remote Sensing Letters* **15**, 1437-1440 (2018).

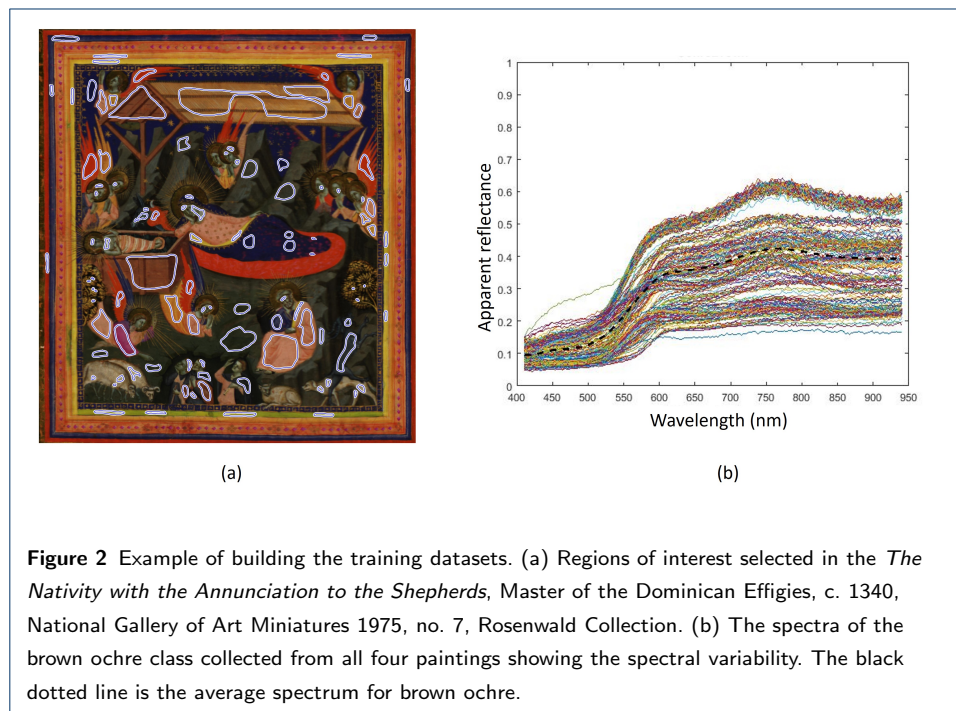
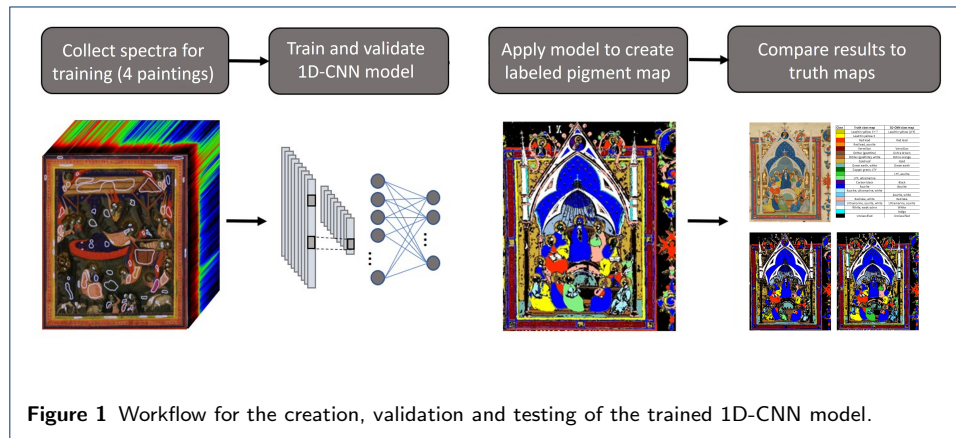
- 753 25. T. Kleynhans, D. Messinger, J. Delaney, Towards automatic classification of diffuse reflectance image cubes
754 from paintings collected with hyperspectral cameras. *Microchemical Journal* **157**, 104934 (2020).
- 755 26. Y. Zhao, R. Berns, L. Taplin, J. Coddington, An investigation of multispectral imaging for the mapping of
756 pigments in paintings. *Proceedings SPIE 6810* (2008).
- 757 27. Y. Zhao, R. Berns, Y. Okumura, L. Taplin, C. Carlson, Improvement of spectral imaging by pigment mapping.
758 *Final Program and Proceedings - IS and T/SID Color Imaging Conference* (2005).
- 759 28. Fiber optics reflectance spectra (FORS) of pictorial materials in the 270-1700 nm range.
760 <http://fors.ifac.cnr.it/>, Accessed: 3 June 2020.
- 761 29. A. Mounier, F. Daniel, Hyperspectral imaging for the study of two thirteenth-century Italian miniatures from
762 the Marcadé collection, Treasury of the Saint-Andre Cathedral in Bordeaux, France. *Studies in*
763 *Conservation* **60**, S200-S209 (2015).
- 764 30. J. K. Delaney, K. A. Dooley, M. Facini, F. Gabrieli, *MANUSCRIPTS in the MAKING: Art and Science*
765 (Brepols Publishers, Fitzwilliam Museum in association with the Departments of Chemistry and History of Art
766 University of Cambridge, (2018).
- 767 31. M. Aceto, A. Agostino, G. Fenoglio, A. Idone, M. Gulmini, P. Marcello, P. Ricciardi, J. Delaney,
768 Characterisation of colourants on illuminated manuscripts by portable fibre optic UV-visible-NIR reflectance
769 spectrophotometry. *Analytical Methods* **6**, (2014).
- 770 32. L. Burgio, R. J. H. Clark, R. R. Hark, Raman microscopy and x-ray fluorescence analysis of pigments on
771 medieval and Renaissance Italian manuscript cuttings. *Proceedings of the National Academy of Sciences*
772 **107**, 5726-5731 (2010).
- 773 33. A. Pallipurath, P. Ricciardi, K. Rose-Beers, 'It's not easy being green': A spectroscopic study of green pigments
774 used in illuminated manuscripts. *Analytical methods* **5** (2013).
- 775 34. M. Melo, P. Nabais, M. Guimarães da Silva, R. Araújo, R. Castro, M. Oliveira, I. Whitworth, Organic dyes in
776 illuminated manuscripts: A unique cultural and historic record. *Philosophical Transactions of The Royal*
777 *Society A Mathematical Physical and Engineering Sciences* **374**, 20160050 (2016).
- 778 35. M. Aceto, A. Arrais, F. Marsano, A. Agostino, G. Fenoglio, A. Idone, M. Gulmini, A diagnostic study on folium
779 and orchil dyes with non-invasive and micro-destructive methods. *Spectrochimica Acta Part A: Molecular*
780 *and Biomolecular Spectroscopy* **142**, 159-168 (2015).
- 781 36. L. Kanter, B. Drake Boehm, C. Brandon Strehlke, G. Freuler, C. Mayer Thurman, P. Palladino, *Painting and*
782 *Illumination in Early Renaissance Florence 1300-1450* New York: Metropolitan Museum of Art,
783 (1994).
- 784 37. B. Keene, New discoveries from the Laudario of Sant'Agnese. *Getty Research Journal* **8**, 199-208 (2016).
- 785 38. B. Keene, Pacino di Bonaguida: A critical and historical reassessment of artist, oeuvre, and choir book
786 illumination in Trecento Florence. *Immediations*, **4** No. 4 (2019).
- 787 39. T. Fushiki, Estimation of prediction error by using K-fold cross-validation. *Statistics and Computing* **21**,
788 137-146 (2011).
- 789 40. Y. Szafran, N. Turner, *Techniques of Pacino Di Bonaguida, Illuminator and Panel Painter, in*
790 *Florence at the Dawn of the Renaissance: Painting and Illumination 1300-1350*, C. Sciacca, ed.
791 (Los Angeles: Getty Publications), 335-355 (2012).
- 792 41. C. Patterson Schmidt, A. Phenix, K. Trentelman, Scientific investigation of painting practices and materials in
793 the work of Pacino di Bonaguida. *Florence at the dawn of the Renaissance: Painting and*
794 *illumination 1300-1350*, C. Sciacca, ed. (Getty Publications, Los Angeles), 361-371 (2012).
- 795 42. M. Abadi, A. Agarwal, P. Barham, E. Brevdo, Z. Chen, C. Citro, G. S. Corrado, A. Davis, J. Dean, M. Devin,
796 S. Ghemawat, I. Goodfellow, A. Harp, G. Irving, M. Isard, Y. Jia, R. Jozefowicz, L. Kaiser, M. Kudlur,
797 J. Levenberg, D. Mané, R. Monga, S. Moore, D. Murray, C. Olah, M. Schuster, J. Shlens, B. Steiner,
798 I. Sutskever, K. Talwar, P. Tucker, V. Vanhoucke, V. Vasudevan, F. Viégas, O. Vinyals, P. Warden,
799 M. Wattenberg, M. Wicke, Y. Yu, X. Zheng, TensorFlow: Large-Scale Machine Learning on Heterogeneous
800 Systems (2015). Software available from tensorflow.org.
- 801 43. R. Shivarudhrappa, N. Sriraam, Optimal configuration of multilayer perceptron neural network classifier for
802 recognition of intracranial epileptic seizures. *Expert Systems with Applications* **89** (2017).
- 803 44. S. Amari, S. Wu, Improving support vector machine classifiers by modifying kernel functions. *Neural*

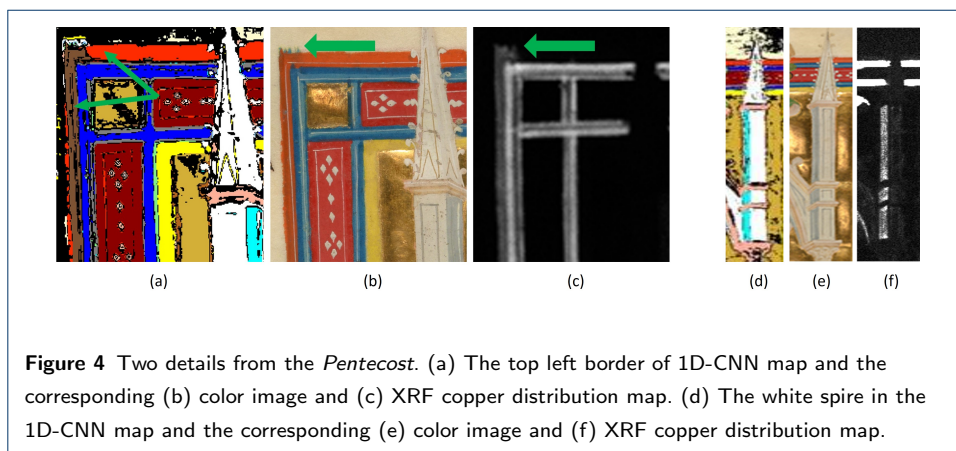
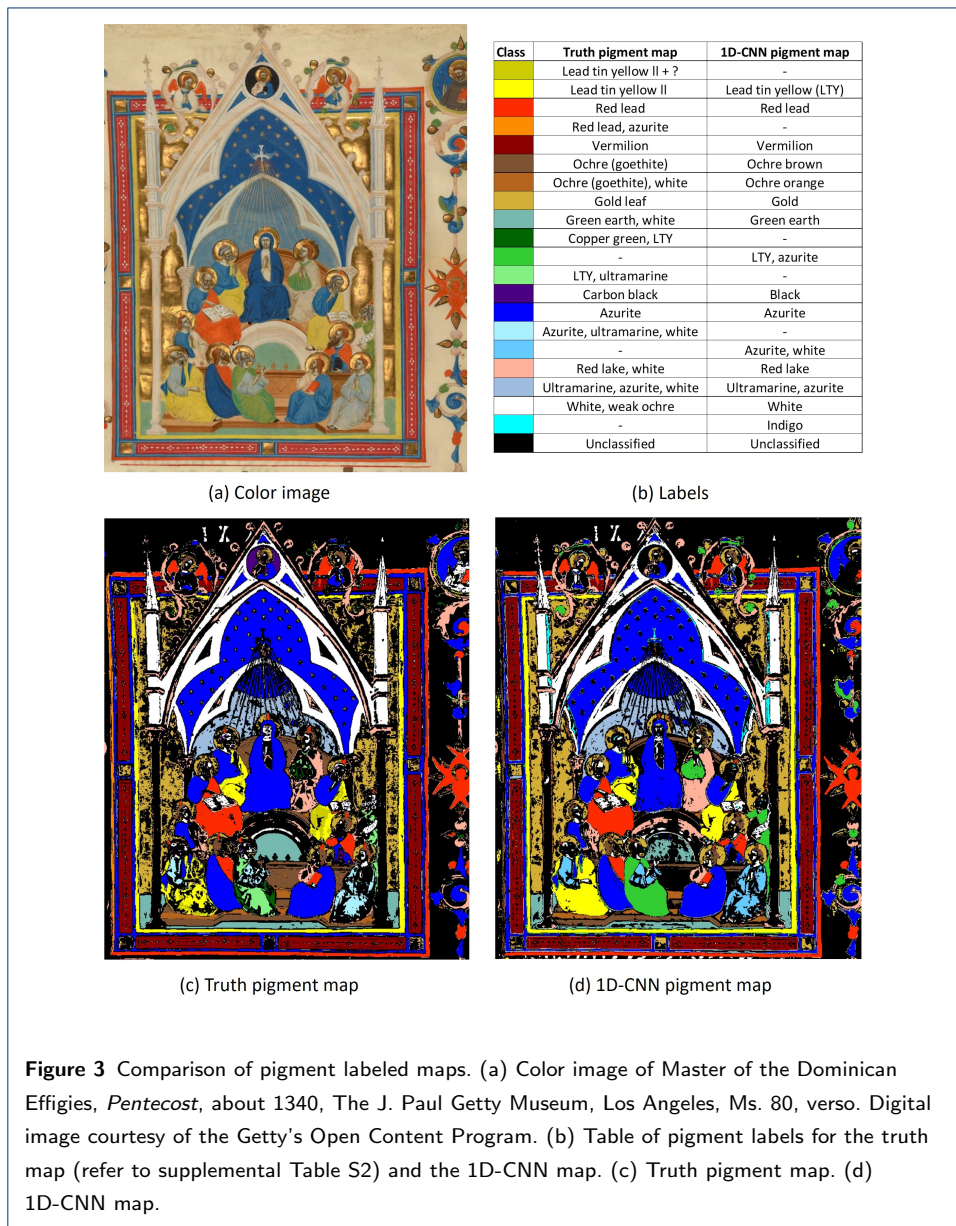
804 *Networks* **12**, 783-789 (2001).

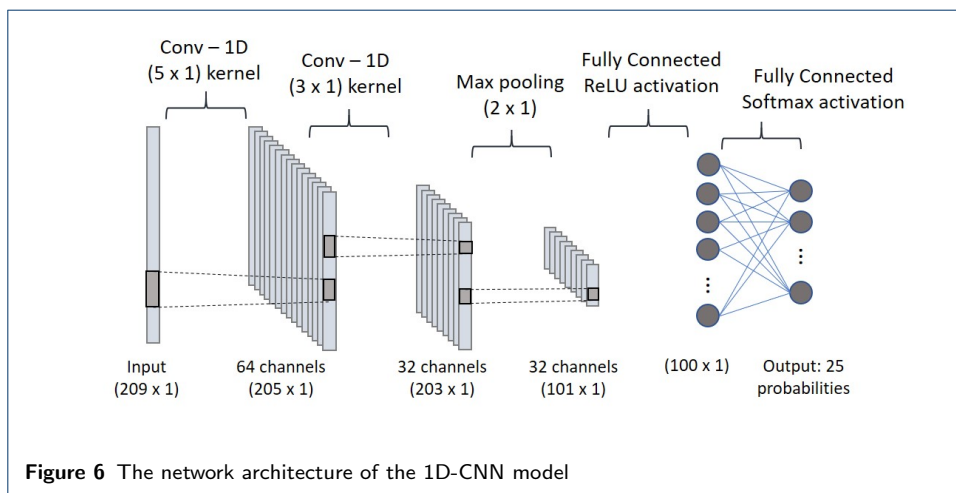
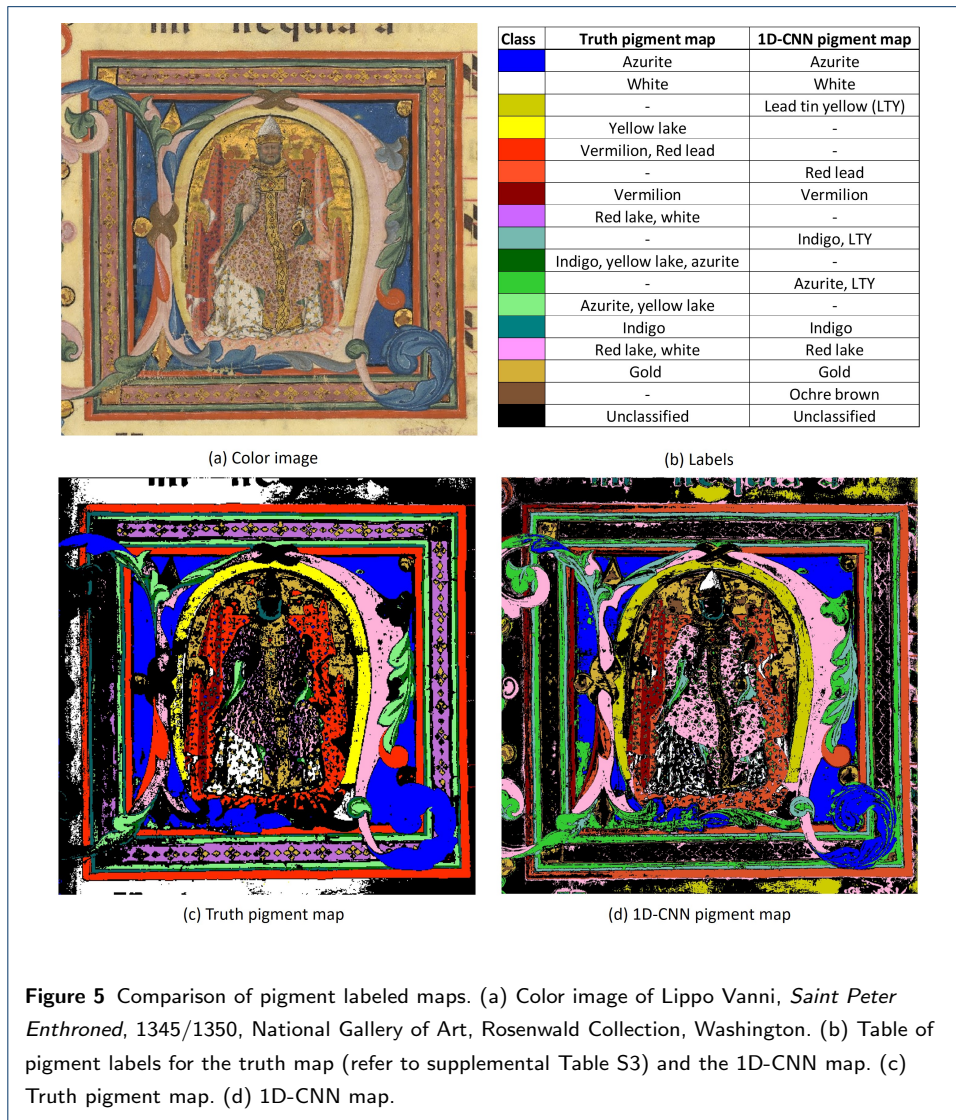
805 45. V. Solé, E. Papillon, M. Cotte, P. Walter, J. Susini, A multiplatform code for the analysis of energy-dispersive
806 X-ray fluorescence spectra. *Spectrochimica Acta Part B: Atomic Spectroscopy* **62**, 63-68 (2007).

807 46. T. Wolff, W. Malzer, I. Mantouvalou, O. Hahn, B. Kanngießer, A new fundamental parameter based calibration
808 procedure for micro x-ray fluorescence spectrometers. *Spectrochimica Acta Part B-atomic Spectroscopy*
809 **66**, 170-178 (2011).

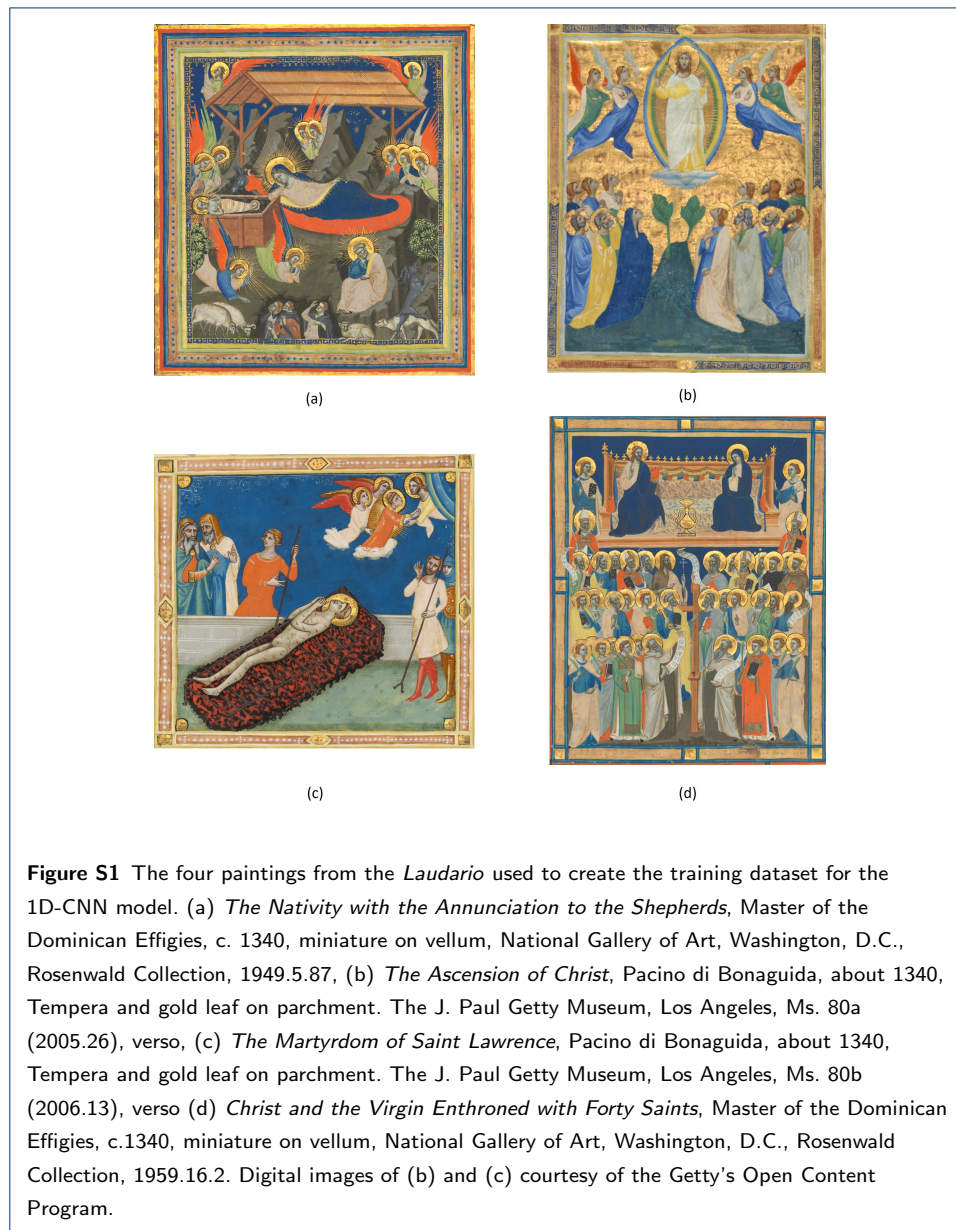
810 **Figures**





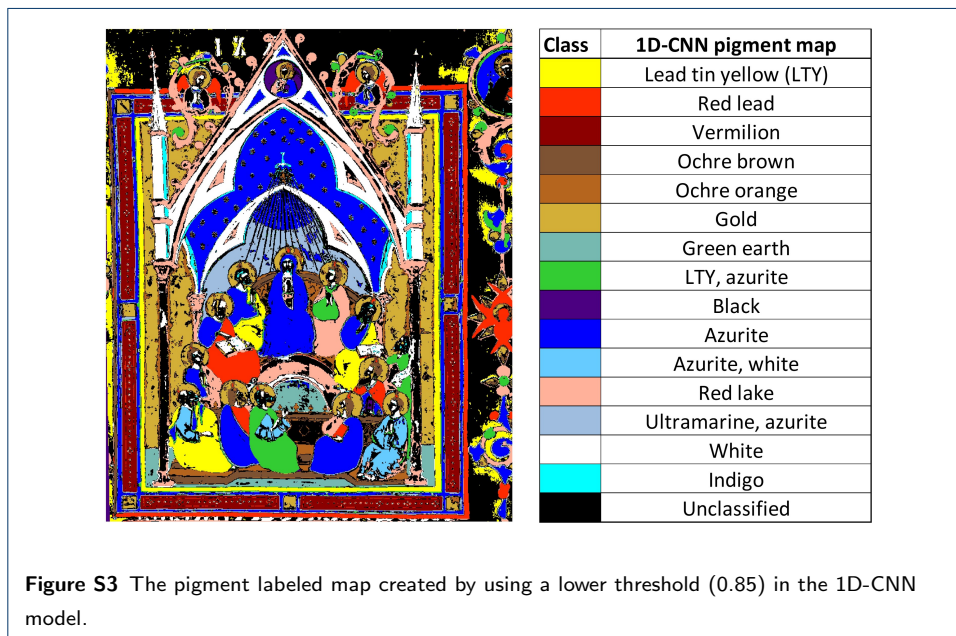
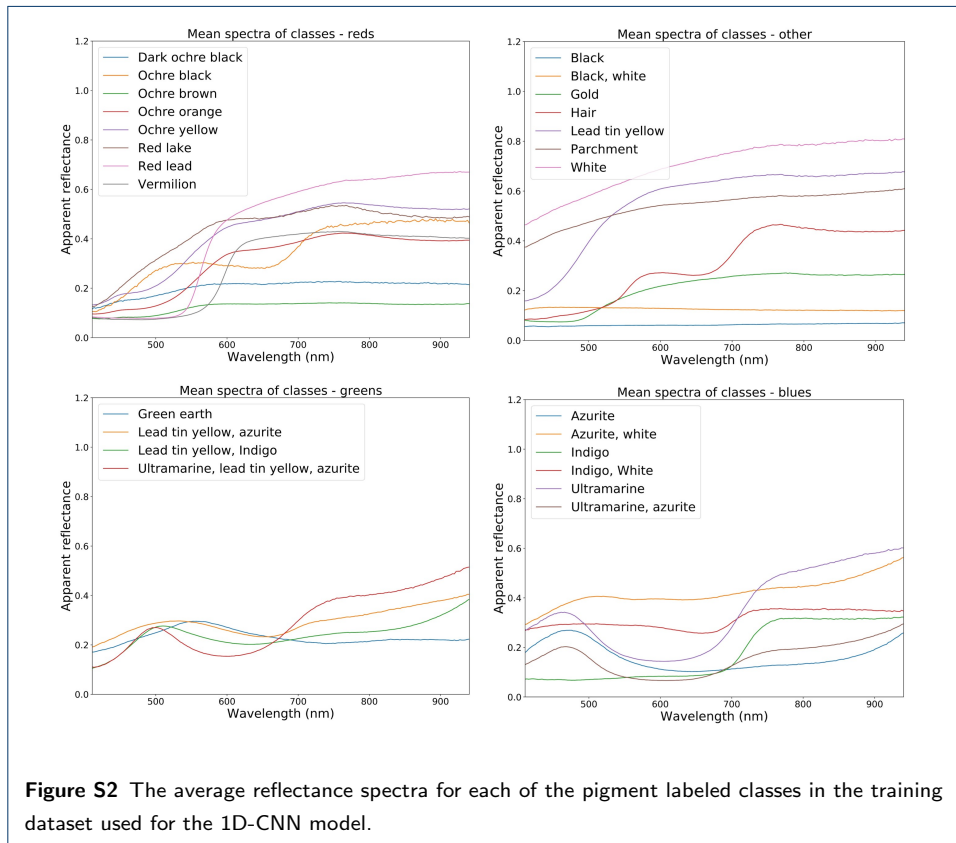


811 Additional Files



Pigment Labels	Accuracy (%)	Total class size
Azurite	100	2047
Azurite, white	100	260
Black	95	94
Black, white	94	130
Dark Ochre Black	100	343
Gold	100	37
Green earth	100	40
Hair	99	166
Indigo	96	55
Indigo, white	100	66
Lead tin yellow, indigo	100	1208
Lead tin yellow	100	978
Lead tin yellow, azurite	100	3495
Ochre black	100	234
Ochre brown	98	801
Ochre orange	98	731
Ochre yellow	89	43
Red lead	100	1030
Ultramarine	100	1324
Ultramarine, Azurite	100	982
Ultramarine, lead tin yellow, azurite	100	48
Vermilion	98	152
White	100	769
Parchment	100	1054
Red lake	100	596
Average accuracy	98.7	16683

Table S1 Summary of per class accuracy for the 1D-CNN model. The 25 pigment/mixture classes and their total class size is given along with the per class accuracy using 10-fold cross validation.

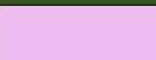


visible paint color	RIS endmember color	RIS endmember features (manual work-up)†	FORS features	XRF (point and/or scanning modalities)‡	Raman	Overall paint composition	Pigment class (likely to be observable in RIS datacube)
yellow		R _{inf} 488 nm, R _{inf} 689 nm, refl hump 738 nm, abs weak 806 nm;		Pb, Sn, Sr, K		lead tin yellow type II	lead tin yellow II +?
yellow		R _{inf} 488 nm, R _{inf} 689 nm,	R _{inf} 490 nm, R _{inf} 689 nm, hump ~725 nm; 1944 nm abs, 2044, 2181 nm	Pb, Sn, Fe, K, Ca/Sr	lead tin yellow type II, vermilion	lead tin yellow type II with trace vermilion	lead tin yellow II
orange-red		R _{inf} 564 nm	--	Pb, C, Cu, Fe	red lead	red lead	red lead
orange-red		R _{inf} 558 nm, turns up at ~850 nm	--	Pb, Cu, Ca	--	--	red lead, azurite
bright red		R _{inf} 602 nm, weak abs 806 nm	--	Hg, S; Pb in the white dots, Fe, (Cu)	vermilion, lead white	vermilion with lead white accents	vermilion
dark brown		abs 485 nm, R _{inf} 457 nm, refl max 757 nm, abs 916 nm	abs ~478 nm, R _{inf} 556 nm, R _{max} 775 nm, abs 905 nm	Fe, Pb, Zn, Cu, S	goethite, lead white	iron earth pigment(s), lead white	ochre (goethite)
light brown		similar to above but offset	--	Pb, Fe, Mn, Zn, Sr	--	iron earth, lead white	ochre (goethite), white
gold		refl ramps 400-478 nm and rounds up (convex (0.3-0.85 %)) broad abs 820 nm	--	Au, Pb (Ca/Sr, Fe, S)	--	gold leaf, iron earth bole, calcium gesso	gold leaf
mint green		R _{max} 542 nm, sh 487 nm, abs 743 nm, w refl at 850 nm, weak abs 919 nm	R _{max} 539 nm, sh 485 nm, abs 750nm, R _{max} 846-855 nm, slow rise at 1100 nm, broad abs at 1443 nm, 1942 nm, 2042, 2182 nm, weak abs 2352, ~2300, and ~1500 nm	Fe, Pb, K, Cu, Ca/Sr, Mn	--	lead white, iron earth pigment(s), trace azurite	green earth, white
dark green		R _{max} 525 nm, broad abs 702 nm	R _{inf} 472-480 nm, R _{max} 525-539 nm, broad abs 680-800 nm with rise to 1329 nm, 1939 nm, 2043, 2181 nm	Pb, Cu, Sn, Fe, Ca/Sr	calcite, lead tin type yellow II, ultramarine	copper green, lead tin yellow type II, ultramarine, calcite	copper green, lead tin yellow
khaki green		R _{inf} 471 nm, R _{max} 524 nm, abs 638 nm, rise, weak abs 803 nm	R _{inf} 476, R _{max} 536-548 nm, abs 642-667 with R _{inf} 695-704, broad abs ~750 nm with rise to 1300 nm, 1939 nm, 2043, 2181 nm	Pb, K, Sn, Cu, Fe, Ca/Sr	calcite, lead tin type yellow II, ultramarine	calcite, lead tin type yellow II, ultramarine, some azurite /copper green and indigo also possible	lead tin yellow, ultramarine/indigo, copper green
black		Refl < 5.2 % +/- 0.4%	--	Ca, K, Sr	carbon black	carbon or bone black	black
dark blue		R _{max} 460 nm, broad abs 638 nm, rapid rise begins at ~860 nm	R _{max} 459 nm, abs 1499, 2287, 2356, 2045 nm; abs 2180 nm, abs 2212	Cu, Pb, Zn, Mn, K, Fe, Ca/Sr (Au)	azurite, lead white, calcite	azurite, with some lead white; gold accents in area behind Virgin	azurite
blue		R _{inf} 444 nm, R _{max} 507 nm, narrow abs 567 nm, broad abs ~600 nm, small peak at 748 nm	R _{max} 491 nm, broad abs 600 nm, broad sh. 731 nm, abs 2286, 2354 nm. Abs 2044, 2181 nm	Pb, Cu, Ca/Sr, Fe, Zn	azurite, ultramarine, lead white, calcite	azurite, ultramarine, lead white, calcite	azurite, ultramarine, white
pink		abs 560 nm (stronger in some areas), vw abs 802 nm	--	(Cu), Pb, Ca/Sr, Fe, Zn	lead white, calcite, gypsum, vermilion	organic red colorant, lead white, calcite, gypsum, trace vermilion	unknown red lake, white
pale blue		R _{max} 483 nm, strong abs 633 nm, shoulder 748 nm, rapid rise after 811 nm	R _{max} 485nm sh. 736 nm; abs 1499, 2287, 2356, 2045 nm; abs 2180 nm, weak abs 2212	Pb, Cu, Ca/Sr, Mn, Zn, Fe	azurite, ultramarine, calcite, lead white	azurite, ultramarine, calcite, lead white	azurite, ultramarine, white
white		convex rise with vw abs at ~485 nm, 800 nm	abs ~478 nm, R _{inf} 556 nm, R _{max} 775 nm, abs 905 nm	Pb, Zn, Mn, Cu, Fe, Ca/Sr, (Au)	lead white, carbon vermilion	lead white, sometimes with small amounts of carbon or vermilion	white, weak ochre (goethite)

† R_{inf} = inflection point, reflection spectrum; R_{max} = local reflection maximum ; refl = reflection; abs = absorption

‡ **Bold** indicates major species, normal text indicates minor species; *italics* indicate trace amounts; (parenthesis) indicates likely from nearby or reverse rather than primary paint color; Relative amounts are estimated as a guide based on peak intensity only.

Table S2 Summary of analyses, the *Pentecost*. Note that the RIS features listed are those identified by an expert user following manual data exploration. When available, fiber optic reflectance spectroscopy (FORS) and Raman analysis may provide additional information about the total chemical composition of each area. However, not all pigments identified are discernible in the RIS data cube on which the 1D-CNN is applied. Therefore, a simplified "pigment class" column notes the materials that should be identified in the paint by this technique.

visible paint color	RIS endmember color	RIS endmember features (manual work-up)†	FORS features	XRF (point and/or scanning modalities)§	Overall paint composition	Pigment class (likely to be observable in RIS datacube)
blue		R_{max} 467-476 nm (light 497 nm) abs 640 nm, R_{inf} increases at 840 nm	R_{inf} 467 nm, abs 1497, 2289, 2352 nm	Cu, Pb (Hg, Fe, As)	Azurite , lead white, (from nearby: vermilion) iron earth	Azurite
white		broad increasing reflectance 400 to 950 nm	broad increasing reflectance 350 to ~1000 nm; weak abs at 1445 nm compared to vellum site	Pb	Lead white	white
yellow		1st derivative: R_{max} 488 nm, FWHM ~120 nm	R_{inf} 486 with sh. 558 (FWHM 160 asym.) (yellow), abs. 2310 (lipid?)	Pb, Hg (Fe, Cu)	Lead white, yellow lake (vermilion from music line reverse side)	yellow lake, white
red/orange		1st derivative: R_{max} 574-580, FWHM ~60 nm	<i>1st derivative, broad with peaks at ~564 and 589 nm, FWHM 66 nm</i>	Hg, Pb	Vermilion, red lead	Vermilion, red lead
green		R_{max} ~517-527nm, abs broad 640 nm, shallow abs 740 nm	R_{max} 520 (green color), R_{inf} 478 (yellow), abs. 647 with R_{inf} 703 (indigo?), broad abs. 600-900 with R_{inf} 959 & abs. 1497, 2284, 2352 (azurite)	Cu, Pb	azurite, organic yellow pigment	azurite, yellow lake
dark green		R_{max} ~510 to 518 abs broad 660 nm, R_{inf} 705 nm	R_{max} 513 (green color), R_{inf} 480 (yellow), abs. 657 with R_{inf} 710 (indigo?), broad abs. 600-900 with R_{inf} 956 & abs. 1496, 2285, 2352 (azurite)	Cu, Pb	indigo/ultramarine (I lean toward indigo), azurite, organic yellow pigment	indigo, yellow lake, azurite
red		1st derivative, R_{max} 602 nm, FWHM 45 nm	R_{inf} 600 nm, FWHM 42 nm	--	vermilion	vermilion
purple		1st derivative 598 nm, FWHM 82 nm, asym	abs. 555 with R_{inf} 597 (FWHM 82 asym.) (red lake), abs. 1450 (lead white)	Ca, S (Si, K, Fe, Cu, Pb)	Red lake, purple lake, azurite, iron earth, lead white	red lake, white
dark green		1st derivative R_{max} 723 or 707 nm FWHM 46 or 56 nm		--		indigo
light pink		1st derivative 590-592.5 nm, FWHM 53 nm, asym	abs. 555 with R_{inf} 590 (FWHM 58 asym.) (red lake), abs. 1449 (lead white)			red lake, white
			abs. 555 with R_{inf} 590 (FWHM 58 asym.) (red lake), abs. 1449 (lead white)	Pb, (Hg, Cu, Ca, Fe)		red lake, white
gold		1st derivative R_{max} 514 nm, FWHM ~70 nm		Au, Ca, Fe, Hg (Cu)	Gold, bole, vermilion	gold leaf
		1st derivative R_{max} 530 nm, FWHM ~50 nm	R_{inf} 533 (FWHM 105 asym.)	S, Sn, Fe, Cu, Zn, Pb (Si), Ca	Mosaic Gold with lead white decorations	mosaic gold

† R_{inf} = inflection point, reflection spectrum; R_{max} = local reflection maximum ; refl = reflection; abs = absorption

§ **Bold** indicates major species, normal text indicates minor species; *italics* indicate trace amounts; (parenthesis) indicates likely from nearby or reverse rather than primary paint color; Relative amounts are estimated as a guide based on peak intensity only.

Table S3 Summary of analyses, *Saint Peter Enthroned*. Note that the RIS features listed are those identified by an expert user following manual data exploration. When available, fiber optic reflectance spectroscopy (FORS) analysis may provide additional information about the total chemical composition of each area. However, not all pigments identified are discernible in the RIS data cube on which the 1D-CNN is applied. Therefore, a simplified “pigment class” column notes the materials that should be identified in the paint by this technique.

Figures

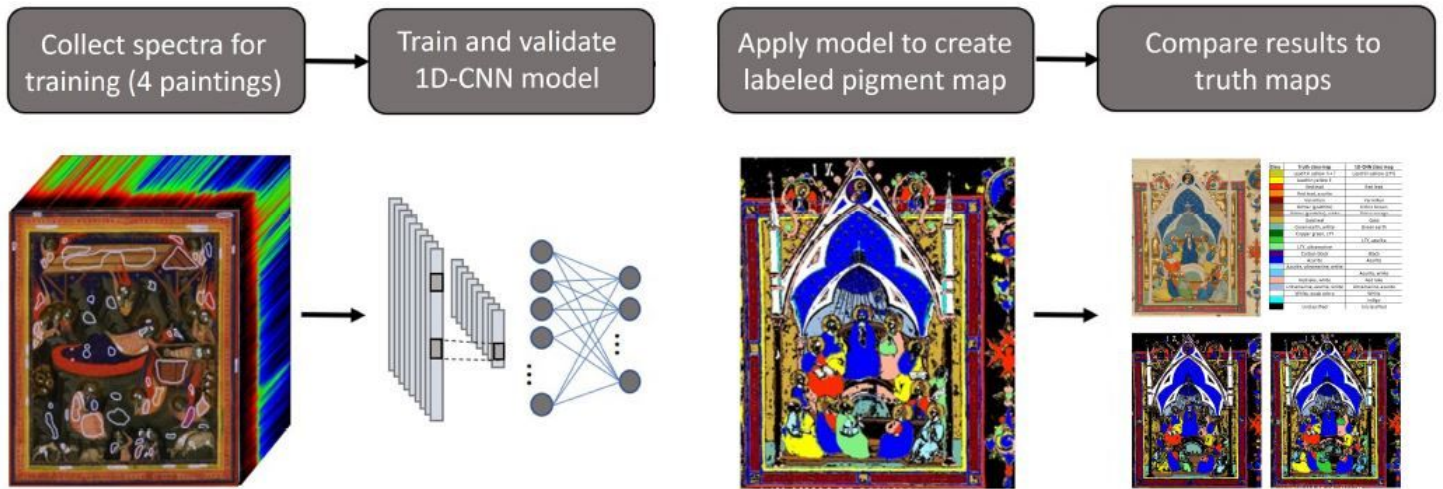
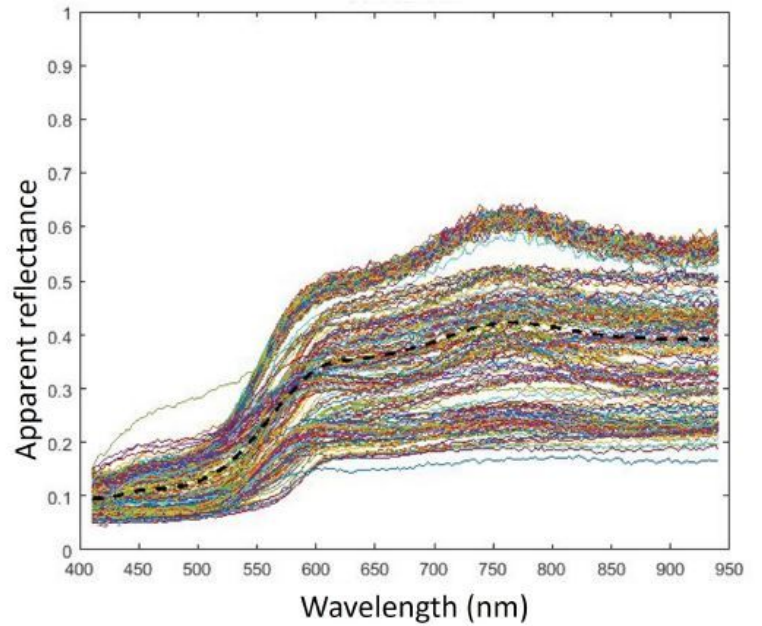


Figure 1

Work ow for the creation, validation and testing of the trained 1D-CNN model.



(a)



(b)

Figure 2

Example of building the training datasets. (a) Regions of interest selected in the The Nativity with the Annunciation to the Shepherds, Master of the Dominican Eægies, c. 1340, National Gallery of Art Miniatures 1975, no. 7, Rosenwald Collection. (b) The spectra of the brown ochre class collected from all

four paintings showing the spectral variability. The black dotted line is the average spectrum for brown ochre.



(a) Color image

Class	Truth pigment map	1D-CNN pigment map
	Lead tin yellow II + ?	-
	Lead tin yellow II	Lead tin yellow (LTY)
	Red lead	Red lead
	Red lead, azurite	-
	Vermilion	Vermilion
	Ochre (goethite)	Ochre brown
	Ochre (goethite), white	Ochre orange
	Gold leaf	Gold
	Green earth, white	Green earth
	Copper green, LTY	-
	-	LTY, azurite
	LTY, ultramarine	-
	Carbon black	Black
	Azurite	Azurite
	Azurite, ultramarine, white	-
	-	Azurite, white
	Red lake, white	Red lake
	Ultramarine, azurite, white	Ultramarine, azurite
	White, weak ochre	White
	-	Indigo
	Unclassified	Unclassified

(b) Labels



(c) Truth pigment map



(d) 1D-CNN pigment map

Figure 3

Comparison of pigment labeled maps. (a) Color image of Master of the Dominican E \tilde{g} gies, Pentecost, about 1340, The J. Paul Getty Museum, Los Angeles, Ms. 80, verso. Digital image courtesy of the Getty's

Open Content Program. (b) Table of pigment labels for the truth map (refer to supplemental Table S2) and the 1D-CNN map. (c) Truth pigment map. (d) 1D-CNN map.

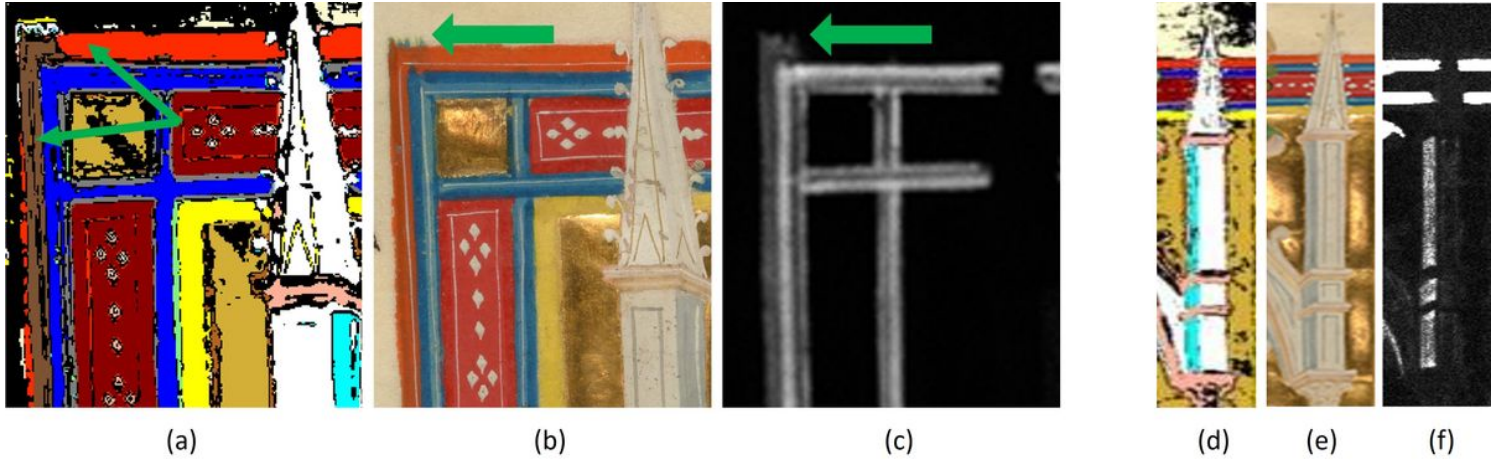
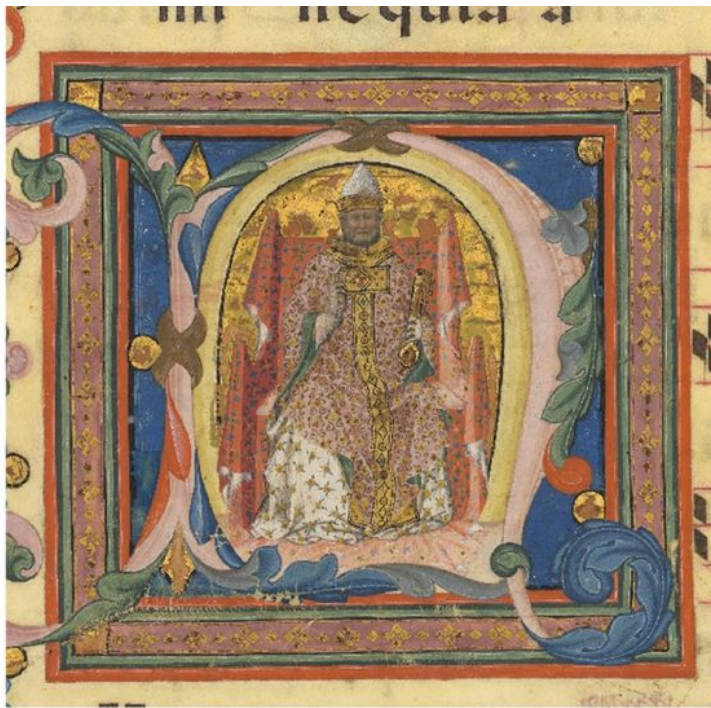


Figure 4

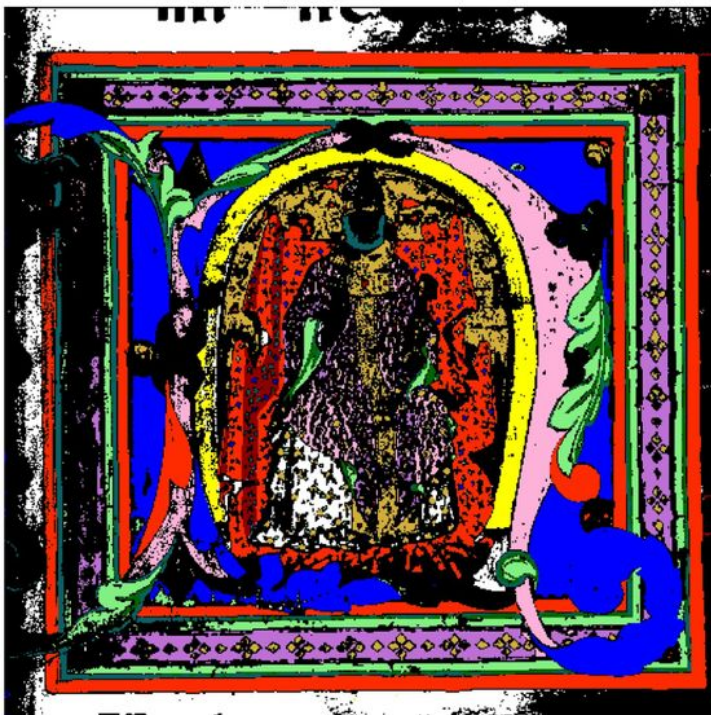
Two details from the Pentecost. (a) The top left border of 1D-CNN map and the corresponding (b) color image and (c) XRF copper distribution map. (d) The white spire in the 1D-CNN map and the corresponding (e) color image and (f) XRF copper distribution map.



(a) Color image

Class	Truth pigment map	1D-CNN pigment map
	Azurite	Azurite
	White	White
	-	Lead tin yellow (LTY)
	Yellow lake	-
	Vermilion, Red lead	-
	-	Red lead
	Vermilion	Vermilion
	Red lake, white	-
	-	Indigo, LTY
	Indigo, yellow lake, azurite	-
	-	Azurite, LTY
	Azurite, yellow lake	-
	Indigo	Indigo
	Red lake, white	Red lake
	Gold	Gold
	-	Ochre brown
	Unclassified	Unclassified

(b) Labels



(c) Truth pigment map



(d) 1D-CNN pigment map

Figure 5

Comparison of pigment labeled maps. (a) Color image of Lippo Vanni, Saint Peter Enthroned, 1345/1350, National Gallery of Art, Rosenwald Collection, Washington. (b) Table of pigment labels for the truth map (refer to supplemental Table S3) and the 1D-CNN map. (c) Truth pigment map. (d) 1D-CNN map.

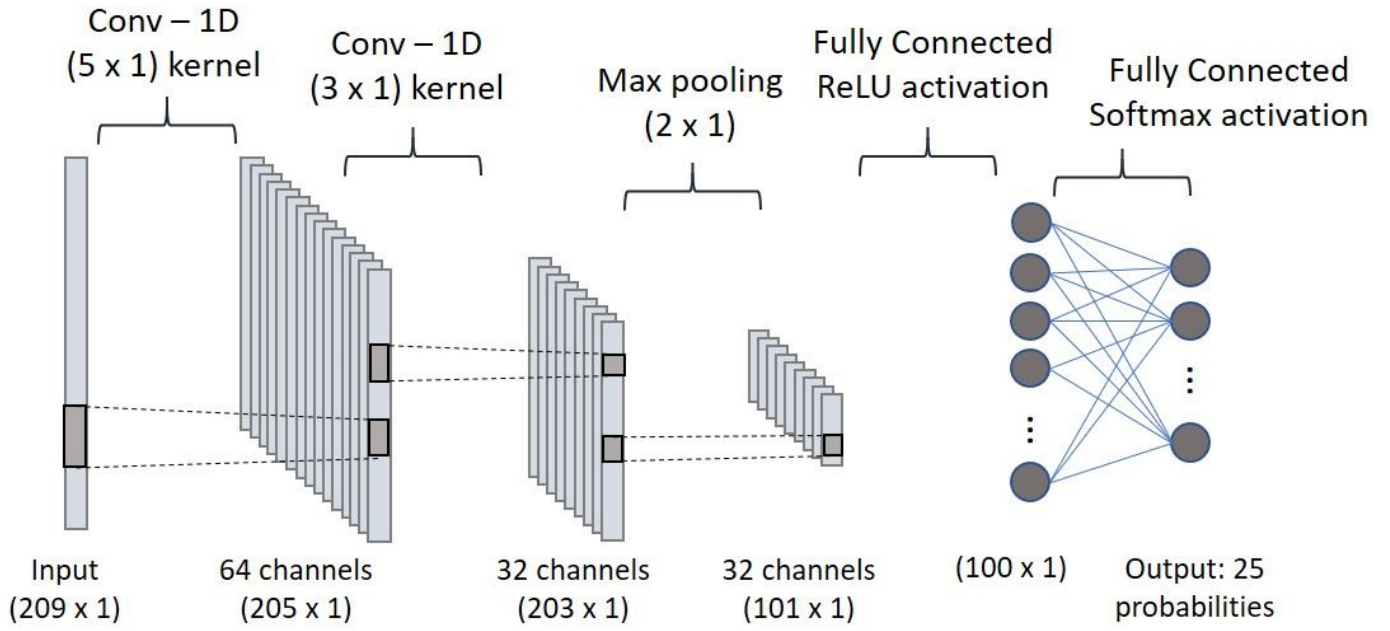


Figure 6

The network architecture of the 1D-CNN model